Journal of Alloys and Compounds 1067 (2026) 188309

Contents lists available at ScienceDirect

Journal of Alloys and Compounds

journal homepage: www.elsevier.com/locate/jalcom

Proton and O vacancy hopping, dopant clustering, and octahedral tilt transitions in exsolved $BaCe_{0.7}Zr_{0.1}Y_{0.15}Ni_{0.05}O_{3-\delta}$

Francesco Cordero [a,*], Floriana Craciun [a], Andrea Brigliadori [b], Andrea Bartoletti [b], Matteo Ardit [c], Pietro Galizia [b], Angela Gondolini [b], Elisa Mercadelli [b,*], Alessandra Sanson [b]

[a] Istituto di Struttura della Materia-CNR (ISM-CNR), Area della Ricerca di Roma - Tor Vergata, Via del Fosso del Cavaliere 100, I-00133 Roma, Italy
[b] Institute of Science, Technology and Sustainability for Ceramics - CNR (ISSMC-CNR), Via Granarolo 64, 48018 Faenza, Italy
[c] Department of Geosciences, University of Padova, v. Gradenigo 6, I-35131 Padova, Italy

ARTICLE INFO

Keywords:
Perovskite
Oxygen vacancy
Proton hopping
Exsolution
Anelasticity
Dielectric spectroscopy

ABSTRACT

Exsolution of metallic nanoparticles from proton-conducting oxides enhances catalytic performance but adds complexity to ionic transport. This study investigates the microscopic processes in $BaCe_{0.7}Zr_{0.1}Y_{0.15}Ni_{0.05}O_{3-\delta}$ (BCZYNi) using dielectric and anelastic spectroscopy under wet and dry conditions, before and after Ni exsolution, with $BaZrO_3$ and $BaCe_{1-x}Y_xO_{3-\delta}$ as reference systems. Elastic anomalies in the complex Young's modulus identify structural transitions driven by oxygen-octahedra tilting, while anelastic relaxation peaks reveal the thermally activated hopping of protons and oxygen vacancies (V_O). In BCZYNi, incomplete hydration (57% of the theoretical limit) is confirmed by the persistence of V_O under wet conditions. Dielectric spectra exhibit near-Debye relaxations with activation energies of 0.51 eV (hydrated) and 0.84 eV (outgassed). The magnitude and timescales of these relaxations suggest long-range transport modes where H and V_O span several lattice spacings, rather than localized dipolar reorientation. The findings demonstrate that dopant clustering is determinant in controlling transport and hydration: while nearest-neighbour dopants trap V_O and suppress hydration, extended dopant aggregates promote locally fast migration of H and V_O without the need for detrapping. Furthermore, a previously unreported dielectric transition near 260 K and the observed structural transition temperatures suggest a role of dopant distribution beyond tolerance-factor predictions.

1. Introduction

The family of yttrium-doped barium cerate–zirconate perovskites (BCZY), as well as co-doped variants, typically with ytterbium (BCZYYb), are currently employed as state-of-the-art high-temperature proton-conducting materials for the fabrication of electrolytes in protonic ceramic fuel cells (PCFCs), protonic ceramic electrolysis cells (PCECs), gas separation membranes and membrane reactors [1–7]. Yb co-doping introduces different defect populations and local structural distortions compared to Y-only doping, which enables modulation of defect association and segregation [8–10]. Ce-rich compositions provide high proton concentrations and enhanced conductivity but are prone to degradation through reaction with H_2O and CO_2, whereas Zr-rich compositions ensure improved chemical stability, particularly their resistance to CO_2-induced decomposition [11], at the expense of increased refractoriness [12–15]. Comparative studies conducted on proton-conducting fuel cells demonstrate that Ce-rich BCZY-based electrolytes outperform pure yttrium-doped barium zirconate (BZY) in terms of power output and area-specific resistance, consistent with their higher proton concentration and lower hole transport numbers [1,2,16]. The highest-performing cells operating at moderate temperatures currently utilize Ce-rich BCZ(Y/Yb) compositions, typically around $BaCe_{0.7}Zr_{0.1}Y_{0.2}O_{3-\delta}$ or $BaCe_{0.7}Zr_{0.1}Y_{0.1}Yb_{0.1}O_{3-\delta}$. These materials exhibit proton conductivities on the order of 1 S cm^{-1} and achieve power densities approaching 1 W/cm^2 under optimized operating conditions [1–4,10]. For example, protonic conductivities as high as 0.19 S cm^{-1} and power densities of 943 mW cm^{-2} have been achieved at 530 °C [4].

Exsolution has recently emerged as a powerful and versatile strategy for tailoring the surface of functional oxides with catalytically active nanoparticles, offering new opportunities in energy conversion and storage [17–19]. Through the optimization of doping strategies and the exsolution process, typically involving thermal treatment under a reducing atmosphere, it is possible to nanodecorate the surface of the materials of interest. In this perspective, exsolution is paving the way for the design of next-generation catalysts and electrocatalysts with improved efficiency and durability, as well as robust ionic conductors

* Corresponding authors.
E-mail addresses: francesco.cordero@ism.cnr.it (F. Cordero), elisa.mercadelli@issmc.cnr.it (E. Mercadelli).

https://doi.org/10.1016/j.jallcom.2026.188309
Received 19 February 2026; Received in revised form 22 April 2026; Accepted 27 April 2026
Available online 29 April 2026

for electrochemical energy conversion and gas separation technologies [20–23]. The exsolution process has historically been employed for the preparation and activation of catalysts and related materials; however, it has only been clearly defined and started to be systematically investigated in recent years [24]. At present, significant knowledge gaps remain regarding the mechanisms governing exsolution, highlighting the need for further in-depth studies beyond conventional microscopy and spectroscopic techniques. As reported, BCZY-based materials find important applications in fuel cells, electrolyzers, and membrane technologies. In modern device modelling, BCZY is treated as a mixed conductor, and a detailed understanding of proton–vacancy dynamics is critical for accurately predicting transport numbers, electronic leakage, and overall efficiency in both fuel cell and electrolysis operating modes [25–28].

The combined use of anelastic and dielectric spectroscopies constitutes a powerful tool for materials investigation, enabling the detailed probing and clear discrimination of protonic relaxations from electronic and vacancy-related processes [29–31]. These techniques further allow the mapping of structural phase transitions and the quantitative assessment of defect association dynamics [31–33]. For instance, systematic studies on the Ce content in BCZY have shown that increasing Ce concentration raises the dehydration temperature and proton concentration, reduces the hole transport number, and enhances oxide-ion conductivity in the 600–700 °C range, thereby strengthening overall ionic transport. This provides a clear explanation for the superior performance of Ce-rich BCZY compositions in PCFCs and PCECs devices [2]. While such investigations have been extensively conducted on $BaCeO_3$, $BaZrO_3$, and related compositions [34–38], they have not yet been carried out in a systematic manner on BCZY and co-doped BCZY materials.

Despite extensive investigations into defect chemistry and transport properties in BCZY-based perovskites, and the recent surge in literature regarding exsolution processes [24,39,40], a comprehensive mechanistic understanding of proton/vacancy dynamics, particularly within exsolved systems, remains elusive [1–4]. In the context of exsolution, most studies still extrapolate defect chemistry and transport behaviour from reference compounds, such as $BaCeO_3$ or $BaZrO_3$ (BZ), rather than on direct experimental measurements of the exsolved BCZY-based materials themselves. In this work, a yttrium- and nickel-co-doped barium cerate zirconate, $BaCe_{0.7}Zr_{0.1}Y_{0.15}Ni_{0.05}O_{3-\delta}$ (BCZYNi), was synthesized via a sol–gel method. The sintered bulk sample was subsequently subjected to an exsolution treatment to nucleate metallic nickel nanoparticles on the surface. The influence of doping and exsolution treatment on vacancies, hydration, relaxation phenomena, and structural phase transitions was thoroughly investigated using anelastic and dielectric spectroscopy on both hydrated and outgassed samples. Relevant insights were obtained regarding the hydration level of Ni-containing samples, tilt transition temperatures, and hypotheses were formulated concerning the distribution of dopant cations in the structure via a nanoscale percolation mechanism.

2. Experimental

2.1. Synthesis of BCZYNi and BZ

Yttrium- and nickel-co-doped barium cerate zirconate (BCZYNi) was synthesized via Pechini sol–gel method from nitrates at 80 °C and pH 9 for 20 h, the procedure was adapted from Barison et al. [8,41]. $Ba(NO_3)_2$ (99%), $Ce(NO_3)_3 \cdot 6H_2O$ (99%), $ZrO(NO_3)_2 \cdot 6H_2O$ (99%), $Y(NO_3)_3 \cdot 6H_2O$ (99%), $Ni(NO_3)_2 \cdot 6H_2O$ (98.5%), ethylenediaminetetraacetic acid (98%), and ethylene glycol (99%) purchased form Sigma-Aldrich and a 30% NH_4OH solution purchased from Carlo Erba were used for the synthesis. $BaCe_{0.7}Zr_{0.1}Y_{0.15}Ni_{0.05}O_{3-\delta}$ perovskite was obtained after a calcination at 1150 ° C for 6 h.

Barium zirconate (BZ) was synthetized using the solid state reaction method, the procedure was adapted from a previous work [42]. $BaCO_3$ (Aldrich purity > 99%) and ZrO_2 (MEL, SC 101, purity > 99%) were used as starting materials, ball-milled for 20 h, then pressed and calcinated at 1300 °C for 5 h. The as produced $BaZrO_3$ perovskite powders were subsequently ball-milled for 100 h and sieved at 250 μm.

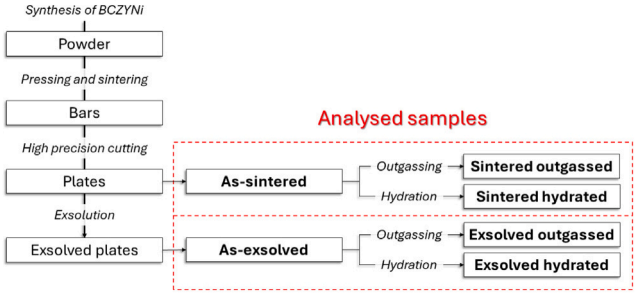

Fig. 1. Schematic representation of the specimens' preparation for the anelastic and dielectric spectroscopies.

2.2. Processing and shaping of BCZYNi and BZ

Calcined powders were pressed and sintered to produce dense bulk materials. Typical plates for anelastic and dielectric spectroscopies were produced by pressing 3.1 g of $BaCe_{0.7}Zr_{0.1}Y_{0.15}Ni_{0.05}O_{3-\delta}$ powder at 1500 kg/cm^2 using a rectangular 40 × 6 mm mould and 8 g of $BaZrO_3$ powder at 180 kg/cm^2 using a rectangular 70 × 7 mm mould. Before the thermal treatment samples were pressed a second time at 2500–3000 bar using a cold isostatic pressing equipment. The sintering process was performed at 1400 °C for 4 h with a heating and cooling ramp of 50 °C/h for BCZYNi and at 1600 °C for 4 h with a heating ramp of 150 °C/h for BZ. To avoid barium loss at high temperatures, the samples were covered with sacrificial commercial BCZY powder [43] and a homemade BZ pack. The sintered bulk BCZYNi underwent a shrinkage during the thermal treatment, obtaining 35 × 5 × 2.5 mm^3 samples, and then they were cut with a high precision cutting machine Berney T34 into 35 × 5 × 0.5 mm^3 specimens for anelastic and dielectric spectroscopies. The sintered bulk BZ sample showed 48.9×5.8×5.8 mm^3 dimension, and then it was cut, in a similar manner for BCZYNi, into 45.7×5.7×0.8 mm^3 and 29.3×5.7×0.8 mm^3 specimens for anelastic and dielectric spectroscopies, respectively.

2.3. Thermal exsolution and surface decoration

$BaCe_{0.7}Zr_{0.1}Y_{0.15}Ni_{0.05}O_{3-\delta}$ plates were treated under reducing atmosphere to trigger the exsolution of nickel metal nanoparticles on the surface of the perovskite. The thermal treatment was performed in a Nabertherm™ Horizontal High-Temperature Tube Furnace - RHTH 120-600/16 using a 5% H_2/Ar ≈ 30 l/h atmosphere, with a 120 °C/h heating rate and 12 h dwell time at 900 °C.

Fig. 1 reports a scheme of the sample preparation procedure and the configurations analysed by means of anelastic and dielectric spectroscopy. Samples labelled as-sintered were BCZYNi plates obtained by cutting sintered bars, whereas as-exsolved samples underwent an exsolution treatment to induce the nucleation of Ni nanoparticles. Both as-sintered and as-exsolved specimens were further conditioned during the temperature runs for the anelastic and dielectric measurements in high vacuum (HV, $<10^{-5}$ mbar), dry or wet atmosphere, to achieve states as fully outgassed or hydrated as possible. In this way, six distinct conditions were investigated: as-sintered, sintered outgassed, sintered hydrated, as-exsolved, exsolved outgassed, and exsolved hydrated.

2.4. XRD

X-ray powder diffraction (XRPD) data were collected using a Bruker D8 Advanced diffractometer operating in Bragg–Brentano geometry. The diffractometer was equipped with a Cu-anode X-ray tube and a LynxEye 1D silicon strip detector (angular range covered by the detector: 3.60° 2θ) set to discriminate Cu$K\alpha_{1,2}$ radiation. A flat fragment of BCZYNi samples ("as-sintered" and "as-exsolved") was placed in a cylindrical specimen holder (27 mm in diameter with an adjustable depth) and scanned in continuous mode over the 20–85° 2θ range, with a step size of 0.02° 2θ and a counting time of 0.5 s per step.

2.5. SEM

The nucleation of Ni nanoparticles on the surface of BCZYNi was investigated by SEM analysis, using a field-emission scanning electron microscope (FE-SEM) ZEISS SIGMA, Carl Zeiss Microscopy GmbH. The instrument was operated at an acceleration voltage of 15 kV and the images were acquired using a secondary electron detector.

2.6. Anelastic spectroscopy

The complex Young's modulus $E = E' + iE''$ was measured by suspending the sample with two thin type K thermocouple wires in vacuum and electrostatically exciting its free-free flexural resonances, as described in [44]. In order to short the thermocouple wires, one of which grounded, and make the sample conductive in correspondence with the exciting/measuring electrode, silver paint was applied to the sample. The Young's modulus is measured from the resonance frequency [45]

$$f = 1.028 \frac{h}{l^2} \sqrt{\frac{E}{\rho}}\ , \tag{1}$$

where l, h, and ρ are the sample's length, thickness, and density, assumed as constants, since they vary much less than E with temperature. The elastic energy loss, $Q^{-1} = E''/E'$, was measured from the decay of the free oscillations, after switching off the excitation, or from the width of the resonance curves. The frequency dependence of the anelastic spectra was measured by exciting 1st and 3rd flexural modes, with frequencies in the ratio 1 : 5.45 [45], during the same run.

Oxygen vacancies (V_O) in perovskites cause anisotropic distortions, called elastic dipoles, in the ideal case of tetragonal symmetry with major axis along the direction of the two nearest neighbour cations. Similarly, the OH groups have orthorhombic elastic dipoles. These elastic dipoles reorient after each jump of V_O or H causing anelastic relaxation, namely Debye peaks in the energy loss measured at frequency $\omega/2\pi$, with maxima at the temperatures such that $\omega\tau \simeq 1$, where τ is close to the mean hopping time [45].

2.7. Dielectric spectroscopy

The complex dielectric permittivity $\varepsilon = \varepsilon' - i\varepsilon''$ was measured with a HP 4284 A LCR metre in a modified Linkam Examina Probe with a sealed volume of ~120 cm^3. When measuring hydrated samples, the volume was left with air, while for outgassed samples it was flushed and filled with N_2.

Similarly to anelastic relaxation, hopping of H causes reorientation of the OH electric dipole and Debye dielectric relaxation. As for V_O, even though they do not have an electric dipole in a regular perovskite ABO_3, the acceptor–V_O complexes certainly have.

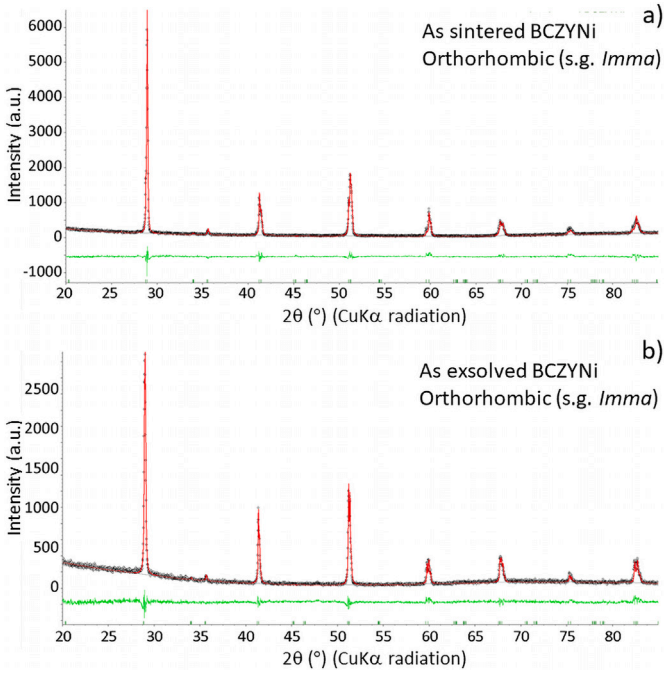

Fig. 2. Rietveld refinement plot of the as-exsolved BCZYNi sample. Black circles represent the experimental data, the continuous red line represents the calculated model, and the lower green curve shows the weighted difference between the observed and calculated profiles. The grey curve corresponds to the fitted background, while the vertical tick marks indicate the Bragg reflection positions of the identified phase.

3. Results

3.1. XRD

3.1.1. Phase identification

Qualitative phase analysis of the collected diffraction patterns, performed using Panalytical HighScore Plus software, revealed that the as-sintered and as-exsolved BCZYNi samples are monophasic and may belong to the monoclinic ($I2/m$) or orthorhombic ($Imma$) crystal systems. Additional data collection was performed in the 15–25° 2θ range to fully ascertain the crystal system. The absence of any reflection in that angular range indicates that the samples are orthorhombic $Imma$ [46]. These results confirm that Ni was successfully incorporated into the perovskite lattice in the as-sintered state, with no detectable segregation of secondary phases such as NiO. Conversely, in the as-exsolved sample, only a fraction of the total Ni content (0.96 wt.%) initially present within the BCZY structure is expected to migrate to the surface [47,48]. Consequently, the exsolved Ni nanoparticles observed via SEM (Fig. 3) remain below the detection limit of XRD; thus, no characteristic peaks for metallic Ni were identified in the diffraction patterns.

3.1.2. Rietveld refinement

The collected XRPD patterns were modelled using the fundamental-parameter Rietveld approach implemented in Bruker TOPAS v.7 software. The instrumental parameters (e.g., goniometer radius, slit sizes, and X-ray tube geometrical parameters) were used to calculate the instrumental contribution to the peak profiles within the fundamental-parameters approach. Starting from the crystal structure of Pagnier et al. [49], the scale factor, unit-cell parameters, and peak profile broadening (modelled using a Lorentzian-type contribution) of the identified perovskite phase were refined. The instrumental zero-error was fixed at the value determined using the NIST Si (640e) standard.

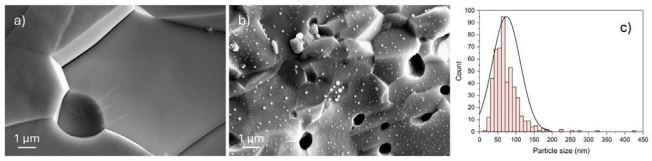

Fig. 3. SEM images of (a) BCZYNi sintered at 1400 °C and (b) BCZYNi after exsolution at 900 °C; (c) particle size distribution of Ni nanoparticles exsolved from BCZYNi.

The refinement included a specimen displacement correction and a five-term Chebyshev polynomial to model the background. The resulting unit-cell parameters are a = 6.1786(2) Å, b = 8.7159(3) Å, c = 6.2085(2) Å, and V = 334.34(2) Å^3, for the as-sintered sample, and a = 6.1746(2) Å, b = 8.7155(6) Å, c = 6.1969(2) Å, and V = 333.49(3) Å^3, for the as-exsolved BCZYNi sample. The crystallite size is 193(19) and 82(5) nm, for the as-sintered and as-exsolved BCZYNi samples, respectively. The refinement agreement factors are: R_{exp} = 0.084, R_{wp} = 0.113, R_p = 0.086, and G.O.F. = 1.34 for the as-sintered sample and R_{exp} = 0.089, R_{wp} = 0.117, R_p = 0.087, and G.O.F. = 1.31 for the as-exsolved sample.

The Rietveld refinement plots for the as-sintered and as-exsolved BCZYNi samples collected at room temperature are shown in Fig. 2.

3.2. SEM

Fig. 3a shows the fracture surface of BCZYNi sintered at 1400 °C, where a relatively flat surface is observed, with no significant surface decorations except for grain boundaries and some residual closed porosity. A comparison with Fig. 3b, which depicts BCZYNi after exsolution at 900 °C, highlights the effect of the thermal treatment under a reducing atmosphere. Nickel spheroidal nanoparticles are homogenously distributed across the grain surfaces; however, a slightly higher concentration of smaller nanoparticles is observed along the grain boundaries. This suggest that grain boundaries act as more effective nucleation sites during the exsolution process. The particle size distribution was estimated to have an average of 74 nm with a broad dispersion (Fig. 3c). In addition, larger particles in the range of 200–500 nm were detected, possibly arising from an imbalance between nucleation and growth kinetics or from the coalescence of multiple nanoparticles. It should be noted that the presence of smaller nanoparticles, below the resolution limit of SEM, cannot be excluded.

3.3. Anelastic spectra

Fig. 4 shows the Young's modulus E normalized at its maximum value of ≃90 GPa and loss Q^{-1} measured in high vacuum exciting the 1st mode (3 kHz, filled symbols) and 3rd mode (16 kHz, open symbols) of BCZYNi during various temperature runs. The peaks of Q^{-1} shift to higher temperature when measured at higher frequency because they are described by expressions of the type of Eq. (2), whose imaginary part is peaked at T_M such that the hopping/reorientation rate τ^{-1} of the free or trapped proton/V_O equals the measuring angular frequency ω, namely $\omega\tau(T_M) \simeq 1$. The initial blue curves of the as-sintered sample are reproducible during heating and cooling until 500 K are not exceeded, while outgassing occurs above that temperature range (see e.g. Fig. 7). The initial anelastic spectrum contains the following features: four thermally activated peaks L1, H1, H2 and H3, which shift to higher temperature at higher frequency, and two phase transitions occurring at the temperatures T_1 and T_2 independent of frequency. The relaxations are classified as high (H) or low (L) based on their temperature and hence activation energy. By comparison with $BaCeO_3$-based materials with similar compositions [31–33], it is anticipated that the phase transitions are due to octahedral tilting, below T_1 from

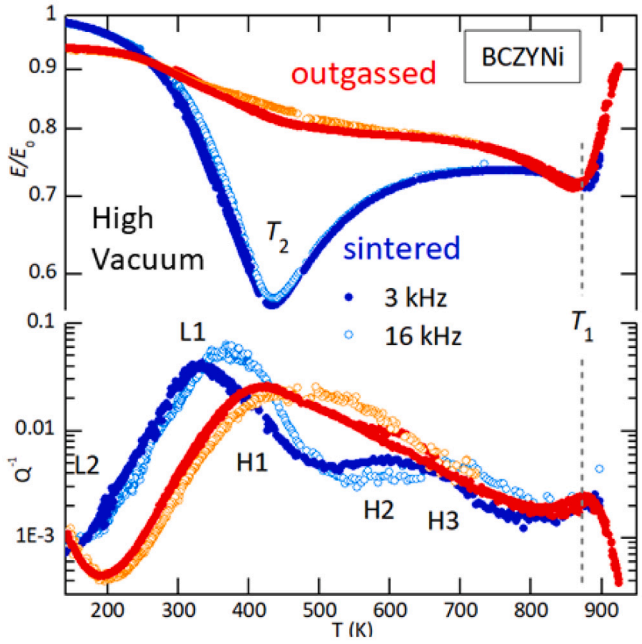

Fig. 4. Young's modulus E and elastic energy loss Q^{-1} measured during several heating and cooling cycles in high vacuum, exciting first and third flexural modes. The blue curves correspond to the initially partially hydrated state after sintering in air, while the red curves are obtained after outgassing up to 940 K.

the cubic phase to a presumably rhombohedral phase and below T_2 to a presumably orthorhombic or monoclinic phase, as discussed later. The red curves measured after having reached the maximum temperature correspond to the outgassed state and are stable during subsequent thermal cycles in vacuum. The loss of H and introduction of V_O depress peak L1, which therefore should be due to H, and enhance peaks H1–H3, therefore attributed to hopping of V_O. In addition, a new peak L2 appears below 200 K, which might be due to small polarons.

The effect of exsolution is presented as curve 3 in Fig. 5 together with the previous curves (1–2, only splines are shown for clarity). Even though the exsolution treatment is expected to completely outgas the sample from H_2O, it appears that a certain hydration level was present, presumably reached during the final cooling step below 200 °C in static atmosphere, and possibly during storage under ambient conditions prior to analysis. The first measurement run was limited to 500 K to avoid outgassing. Both H1 and L1 are clearly visible, indicating that the hydration level was lower than after sintering in air, as expected. The height of H1 alone is not a good indicator of the content of V_O, since it will be explained later that it is enhanced by the tilt transition at T_2, to which the ordering of V_O is coupled. After the exsolution treatment, the amplitude of the softening due to this phase transition is slightly smaller but otherwise little affected. As for peak L2, it behaves as before exsolution: it is absent or strongly depressed in the partially hydrated state and reappears after extending heating to 950 K, with complete outgassing (curve 5). Due to the sample shape and high damping levels, after exsolution the higher frequency could be measured only below room temperature, and reveals that both the L1 and L2 are thermally activated with a broad distribution of activation energies (not shown here).

The remaining features of curve 4 are very similar to curve 2 of the outgassed state prior to exsolution, except for a lower T_1. Other anelastic measurements followed, after hydrating and outgassing treatments, substantially reproducing the previous curves. Curve 5 is the last measurement performed under 20–30 mbar H_2O, corresponding to water saturated air at ambient temperature.

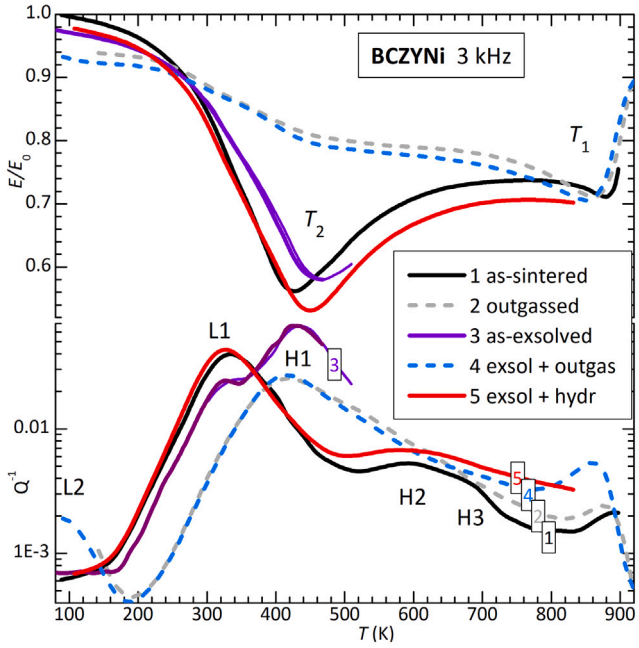

Fig. 5. Young's modulus E and elastic energy loss Q^{-1} in the as prepared state (1), after having reached 924 K in high vacuum (HV), with consequent dehydration (2); after exsolution and partial hydration (3); temperature run up to 750 K (4) and 914 K (5) in HV, with increasing dehydration. All measurements are made in HV except curve 5 in 20–30 mbar H_2O.

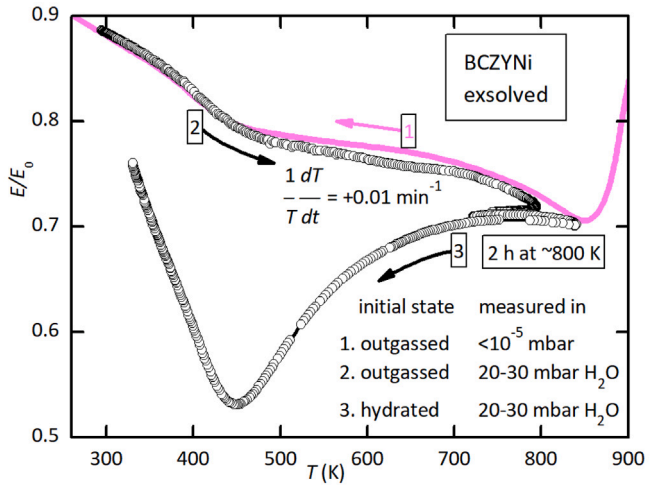

Fig. 6. Young's modulus E of the exsolved outgassed sample (curve 1 corresponding to curve 4 of Fig. 5) during in situ hydration in 20–30 mbar H_2O, up to 840 K and varying T for 2 h around 800 K (curve 2) and final cooling (curve 3 corresponding to curve 5 of Fig. 5).

In principle, only the anelastic spectra in the outgassed state are measured under equilibrium stoichiometry at high temperature in vacuum, while in all other cases there should be exchange of H_2O between sample and atmosphere during the anelastic and dielectric measurements. Yet, it has already been mentioned that during the temperature runs in vacuum there is no appreciable loss of H_2O below 500 K, and Fig. 6 demonstrates that also H_2O absorption in wet atmosphere occurs well above that temperature. The figure presents the evolution of the Young's modulus in the outgassed state (curve 1 corresponding to curve 4 of Fig. 5) during in situ hydration in a static water-saturated atmosphere (20 mbar H_2O at room temperature up to 30 mbar at

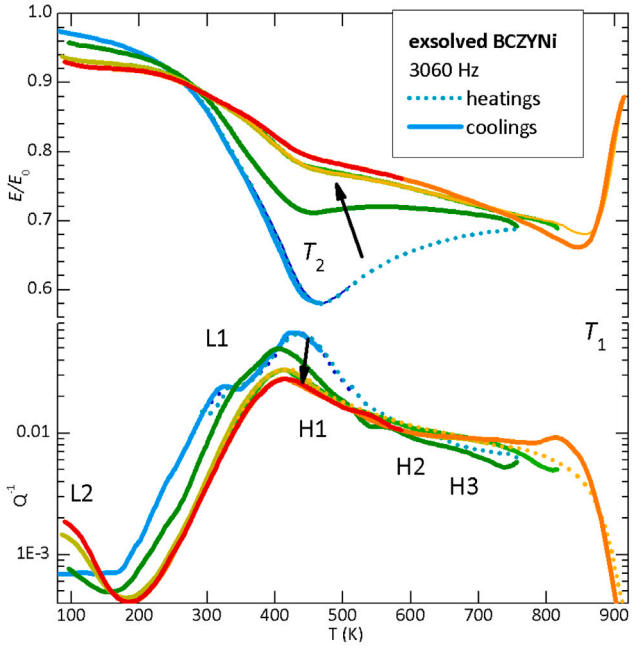

Fig. 7. Series of measurements in high vacuum of the Young's modulus E and elastic energy loss Q^{-1} after exsolution. The arrows indicate the chronology of the runs with increasing maximum temperature.

high temperature). Curve 2 was measured heating at the usual rate of $T^{-1}dT/dt = 0.01$ min^{-1} and remains close to the outgassed state up to nearly 800 K (curve 2). Uptake of water occurs during a 2 h stay around 800 K, varying little temperature until the $E(T)$ curve stabilizes and the fully hydrated cooling curve 3 (corresponding to curve 5 of Fig. 5) is traced. This demonstrates that all the anelastic and dielectric spectra are taken at nearly constant stoichiometries at least up to 700 K.

Fig. 7 shows the evolution of the anelastic spectrum of the exsolved sample during runs up to increasing maximum temperatures, which caused progressive outgassing. The labels H2 and H3 indicate the positions of the these peaks in the as sintered state, where they were more distinguishable.

3.4. Dielectric spectra

The dielectric measurements were performed in a closed volume of 120 cm^3 initially in ambient air when measuring the hydrated sample, and in dry N_2 for the outgassed state, to prevent major outgassing or hydration at high temperature. In view of the results of Fig. 6, the initial hydration state can be considered nearly constant over the whole temperature range. Indeed, the curves in Fig. 8, measured between 200 Hz and 200 kHz during a series of heating and cooling cycles on the as sintered sample, were reproducible. Only the height of the major relaxation peak above room temperature, labelled L1d for analogy with the anelastic spectrum, had a minor variation. An additional minor relaxation labelled L2d, and probably consisting of two components, is found above 100 K, while a phase transition is observed at $T_3 \simeq 267$ K.

The evolution of the dielectric spectrum after exsolution and a final outgassing in vacuum is presented in Fig. 9. The main effect of the exsolution treatment is the disappearance of L2d, similarly to the anelastic L2, while the phase transition and the main relaxations at high temperature are little affected. The measurement after annealing in air at 500 °C is not shown because it overlaps with curve 3.

A drastic change is found in the exolved sample after outgassing for 1.5 h at 700 °C in $<10^{-5}$ mbar, with the loss of 0.0156 mol H_2O. The major relaxation is shifted nearly 100 K to higher temperature and labelled H1d, while the phase transition is shifted 12 K lower

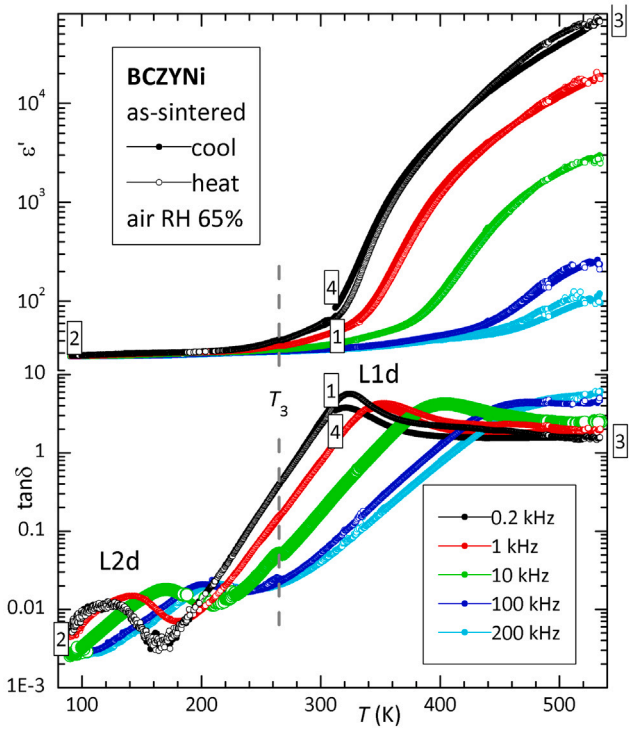

Fig. 8. Dielectric susceptibility, ε' (notice the broken ordinate) and $\tan\delta$, of the as sintered sample. The numbers signal the start of various cooling (closed symbols) and heating (open symbols) runs. The vertical dashed line marks a phase transition during heating.

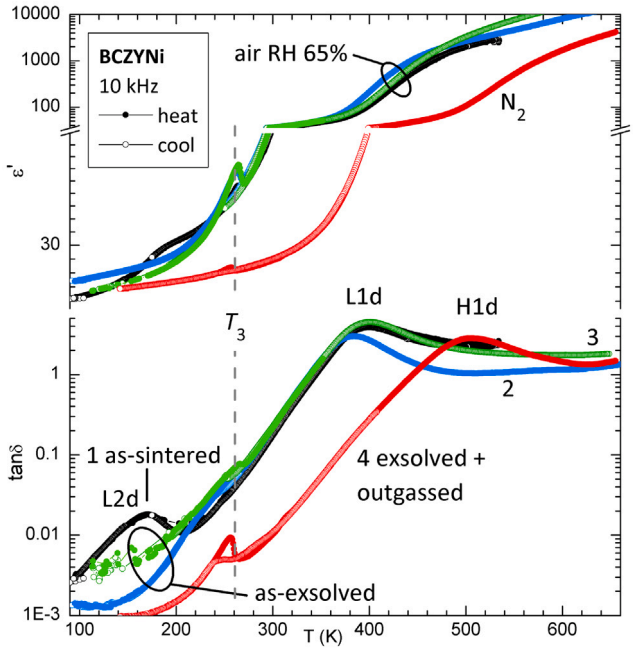

Fig. 9. Dielectric susceptibility, ε' and $\tan\delta$, measured at 10 kHz during heating (open symbols) and cooling (closed symbols) measured after sintering (black), after Ni exsolution (blue and green) and after outgassing (red). The vertical dashed line marks the phase transition during heating.

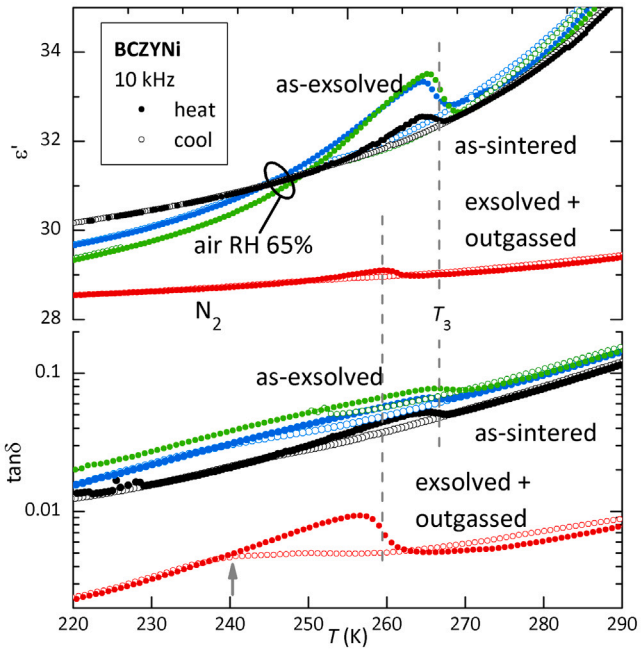

Fig. 10. Enlargement of the curves in Fig. 9 around T_3. The anomaly during cooling is shifted 15–20 K to lower temperature and is particularly evident after outgassing (arrow).

to T_3 = 256 K. The anomaly at T_3 is more evident because of the reduced susceptibility but its amplitude is actually reduced (notice the logarithmic scales). An enlargement of the curves in Fig. 9 around T_3 is shown in Fig. 10, while Fig. 11 shows the amplitudes of the dielectric anomalies during heating in the various states of the sample versus the measuring frequency. The anomaly is also present during cooling, with 15–20 K of thermal hysteresis, but is much less visible, as indicated by the arrow at 240 K.

The amplitude decreases with increasing frequency. If a $\Delta\varepsilon/\varepsilon \sim f^{-n}$ law is assumed, it is $n \simeq 0.4$ in the initial state, $n \simeq 0.14$ after exsolution and $n \sim 0.6$ after the final outgassing, while the frequency dependence of $\Delta\tan\delta$ is less defined.

In view of the conversion of relaxation L1d into H1d after outgassing, we attempted fits to the susceptibility curves before and after outgassing the exsolved sample, to test whether these main relaxations might be due to dipolar relaxation involving H and V_O.

The dielectric spectra have been analysed in terms of two Havriliak–Negami relaxation processes

$$\Delta\varepsilon_i = \frac{\Delta_i}{T}\frac{1}{\left[1+\left(i\omega\tau_i\right)^{\alpha}\right]^{\gamma}} \tag{2}$$

$$\tau_i = \tau_{0i}\exp\left(E_i/k_B T\right) \tag{3}$$

where $\alpha < 1$ symmetrically broadens the Debye relaxation, as in the Cole-Cole distribution, while $\gamma < 1$ broadens the high–$\omega\tau$ / low–T side, plus a phenomenological expression corresponding to the universal dielectric response [50] for the contribution from conductivity [51]

$$\varepsilon_\sigma = \sigma_0\,(i\omega)^{-\beta}, \tag{4}$$

where it should ideally be $\beta = 1$. The global fits of real part and $\tan\delta$ at three frequencies are shown in Figs. 12 and 13 and the corresponding parameters in Table 1, where ε_∞ is the high-frequency permittivity.

For the lowest frequency also the three contributions are separately plotted. Notice that in $\tan\delta$ these contributions are not additive as in ε'', since the relaxation strengths are far larger than the background ε_∞ and therefore ε' in the denominator varies much with temperature. This

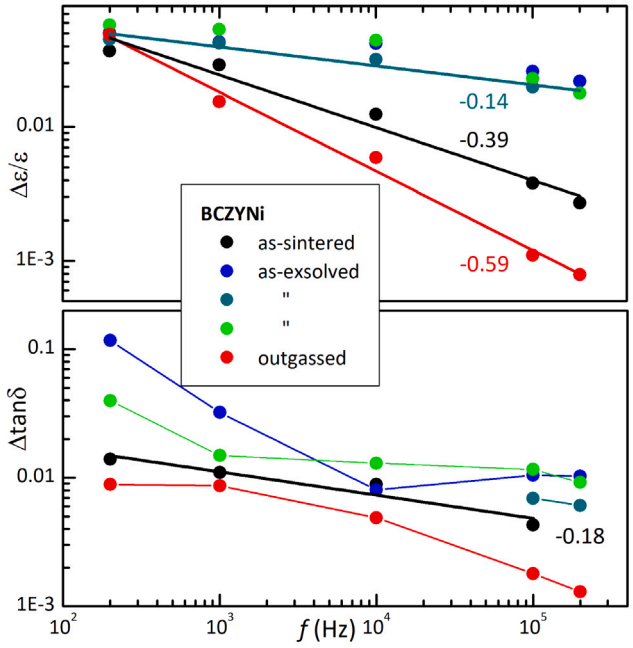

Fig. 11. Amplitude of the dielectric anomaly during heating through T_3 in the various states of the sample (legend in chronological order).

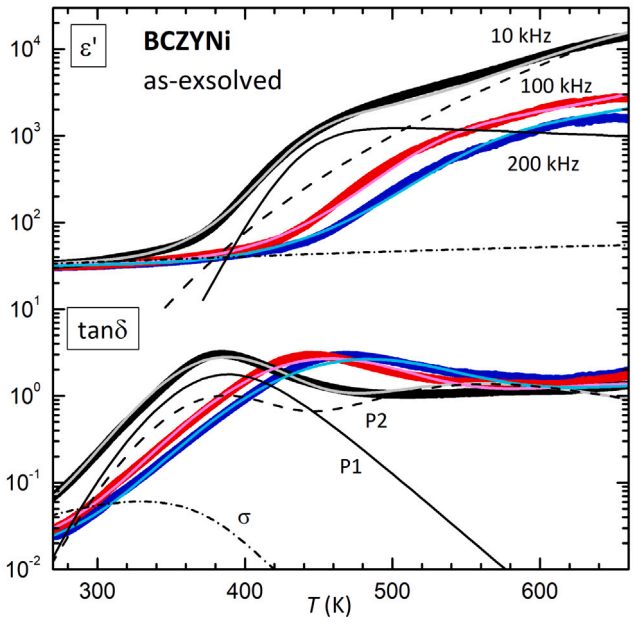

Fig. 12. Fit to the dielectric susceptibility, ε' and $\tan\delta$, measured at 10, 100, 200 kHz after exsolution. The thin lines are the fits, including the three components at the lowest frequency.

explains the fact that the contribution of P2 is also peaked in correspondence with the more intense P1. The contribution from conductivity has β quite smaller than 1, because it helps improving the fit also in the low temperature limit, but is also negligible with respect to the major relaxations.

3.5. Mass gain/loss after hydration/outgassing

The nominally maximum hydration of $BaCe_{0.7}Zr_{0.1}Y_{0.15}Ni_{0.05}O_{3-\delta}$, assuming Ni^{3+}, is 0.1 mol H_2O. The anelastic spectra indicate that

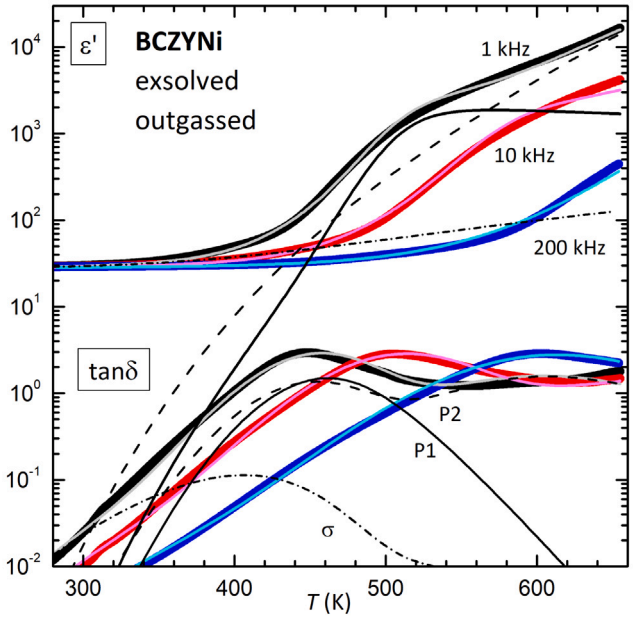

Fig. 13. Fit to the dielectric susceptibility, ε' and $\tan\delta$, measured at 1, 10, 200 kHz after exsolution and outgassing. The thin lines are the fits, including the three components at the lowest frequency.

Table 1
Fitting parameters used in Figs. 12 and 13.

	Exsolved (~wet) P1 ≡ H1d	Exsol+outg P1 ≡ L1d
Δ_1 (K)	6.52×10^5	1.11×10^6
τ_1 (s)	2.40×10^{-11}	8.75×10^{-13}
E_1 (eV)	0.514	0.840
α_1	0.983	0.938
γ_1	1	1
Δ_2 (K)	3.03×10^7	5.06×10^7
τ_2 (s)	6.49×10^{-10}	2.95×10^{-10}
E_2 (eV)	0.614	0.814
α_2	0.764	0.812
γ_2	1	1
ε_∞	30.0	28.3
σ_0 (s^β)	1330	8.73×10^4
E_c (eV)	0.0749	0.210
β	0.234	0.332

complete hydration is never obtained, since peaks H1-H3 are always present. In order to have a quantitative estimate of the hydration level after sintering in air and after exsolution, we measured the mass gain of the two outgassed samples after heating in air to 500 °C, followed by natural cooling, simulating the hydration after sintering. After such a treatment, the as-sintered bar for the anelastic experiments in the completely outgassed state had a mass gain corresponding to 0.0374 mol H_2O, which should be indicative of the hydration level after sintering.

The other sample was subjected to the same annealing in air at 500 °C after exsolution and two dielectric experiments in N_2 atmosphere, which should have roughly preserved the original hydration level after exsolution, and its mass gain corresponded to 0.0147 mol H_2O. A final outgassing for 1.5 h at 700 °C in $<10^{-5}$ mbar caused the loss of 0.0355 mol H_2O, close to hydration level found in the previous sample. We conclude that the hydration level after sintering or heating in air was ~0.035–0.038 mol H_2O, while that after exsolution was ~ 0.02–0.023 mol H_2O, consistent with the relative intensities of peaks L1 and H1 in Fig. 7.

The highest hydration of 0.057 could be reached in the exsolved and outgassed sample, keeping it at 580 °C for 5 h in 26 mbar H_2O,

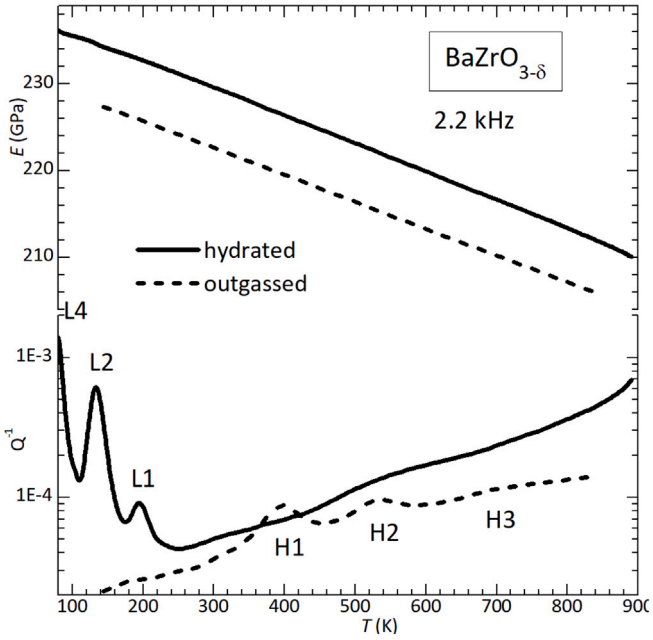

Fig. 14. Young's modulus E and elastic energy loss Q^{-1} of $BaZrO_3$ with acceptor impurities in the as prepared hydrated state (continuous line) and after outgassing (dashed).

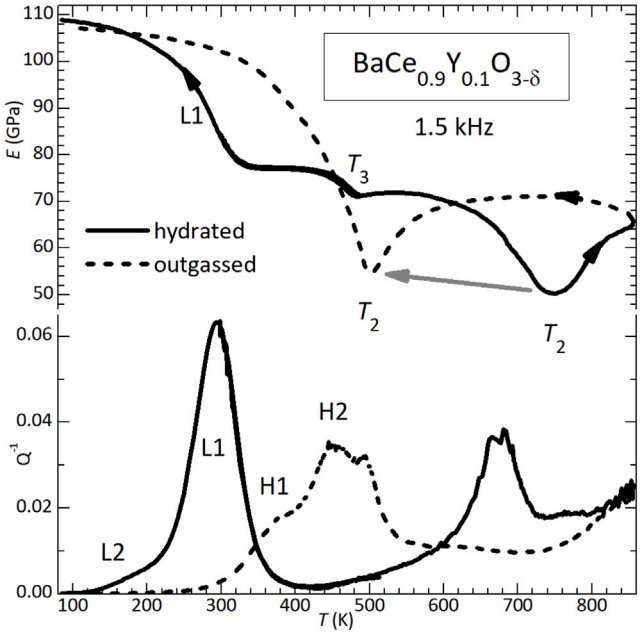

Fig. 15. Young's modulus E and elastic energy loss Q^{-1} of $BaCe_{0.9}Y_{0.1}O_3$ in the hydrated state (continuous line) and after outgassing (dashed) from Ref. [33]. The thermally activated relaxation peaks above (below) room temperature are indicated with H1, H2 (L1, L2). The structural transitions are indicated with T_2 (O/R) and T_3 (O′/O).

corresponding to 100% relative humidity at 24 °C, followed by cooling at 0.7 °C/min.

4. Discussion

4.1. The simpler cases of BZ and BCY: hopping of H and V_O

In order to interpret the anelastic spectra of this rather complex composition it is better to start with related cases that are simpler and better established. The simplest case is $BaZrO_3$, which remains cubic down to 0 K. The sample of Fig. 14 contains acceptor impurities, whose charge imbalance is compensated by V_O in the outgassed state and by H in the hydrated one. Based on the analysis of the starting powder oxides, the major impurity is Fe^{3+} substituting Zr^{4+}, but V_{Ba} are also possible. Correspondingly, the outgassed spectrum contains only peaks H1-H3 above room temperature, due to the hopping of V_O, partly free and partly trapped by more than one type of acceptor impurities, while the hydrated spectrum contains peaks L1–L4 below room temperature, due to the faster hopping of H, at low temperature trapped by the various acceptor types. Since the hopping rate of point defects generally follows the Arrhenius law $\tau = \tau_0 \exp\left(E/k_B T\right)$ with $\tau_0 = 10^{-14} - 10^{-13}$ s, the condition of maximum relaxation $\omega\tau = 1$ at room temperature and ~2 kHz correspond to an activation energies $E \leq 0.37$ eV for the low temperature peaks and ≥0.65 eV for the high temperature peaks, which are reasonable hopping barriers for H and V_O.

The case of $BaCe_{1-x}Y_xO_3$ has been amply discussed [31–33] and Fig. 15 presents the anelastic spectra of BCY10 ($x = 0.1$) in the hydrated and outgassed states. The latter is obtained after heating in HV up to 860 K, which is sufficient to replace peaks L1 and L2 from H hopping with peaks H1, H2 due to V_O hopping. While the hydrated state is stable during measurements in HV up to about 500 K, heating at higher temperature releases H_2O, and therefore the high temperature side of the continuous curve, including the dissipation peak around 680 K, is out of equilibrium, until complete outgassing is achieved.

It has also been observed that, when the measuring frequency increases and peak H2 shifts to higher temperature, its height sharply increases on approaching the transition at T_2 [31]. This is due to a strong coupling with that structural transition, which renders the O sites inequivalent below T_2 and causes partial ordering of V_O over one of the two inequivalent O sublattices [52,53]. This also implies that the height of H2 alone is not indicative of the content of V_O.

4.2. The simpler case of BCY: structural phase transitions

The structural transitions in $BaCeO_3$ and materials with similar compositions are due to tilting and distortions of the O octahedra, which is strongly coupled to strain and therefore causes evident anomalies in the elastic moduli. On the other hand, the rotations of the octahedra in a regular perovskite lattice are non polar and therefore can cause only minor dielectric anomalies by coupling with existing defect dipoles. Notice that in an undoped perovskite V_O do not have an electric dipole.

The sequence of transitions in $BaCeO_3$ is, starting from high temperature: cubic $Pm\bar{3}m$ (C), rhombohedral $R\bar{3}c$ (R), orthorhombic Imma (O), orthorhombic $Pnma$ (O′) [52–54], which is peculiar because in most perovskites the ground state is $R\bar{3}c$ with a antiphase rotations about all three O-B-O axes with the same magnitude. Accordingly, the phase transitions appearing as elastic anomalies in $BaCe_{1-x}Y_xO_3$ have been assigned as $C \overset{T_1}{\rightarrow} R \overset{T_2}{\rightarrow} O \overset{T_3}{\rightarrow} O'$ [33]. From Fig. 15 it also appears that outgassing causes a huge shift of the transition between R and O phases to lower temperature: T_2 passes from ≥750 K to 500 K. This is evident from the continuous shift of T_2 with increase of the level of outgassing [31–33], shown here only for the fully hydrated and outgassed cases with $x = 0.1$, while with $x = 0.2$ the shift is even of ~300 K. The dependence on the level of hydration of the temperatures of the transitions involving octahedral tilting in BCY has been confirmed by neutron diffraction [55].

This behaviour can be interpreted as arising from octahedral tilting in $A^{2+}B^{4+}O_3$ perovskites being induced by the mismatch between the B–O–B and A–O–A sublattices [56]. The latter is made of longer, weaker and therefore more anharmonic bonds, which shrink more during cooling, until the pressure exerted on the more rigid BO_6 octahedra

induces their rotation without need of shrinking [31,33]. The mismatch is usually expressed in terms of the tolerance factor [56]

$$t = \frac{r_A - r_O}{\sqrt{2}\,(r_B - r_O)} \tag{5}$$

with the Shannon ionic radii [57]. Perfect matching with the cubic structure is obtained with $t = 1$, while $t < 1$ indicates a tendency to tilt, and one can phenomenologically define a threshold t below which similar perovskites undergo octahedral tilting below a same temperature. The V_O introduced by outgassing weaken the mismatch between the B-O-B and A-O-A networks, which remain untilted down to lower temperature. In $BaCe_{1-x}Y_xO_{3-\delta}$ it is possible to interpret the dependence of T_2 on δ defining an effective tolerance factor in the presence of vacancies [31,33].

4.3. BCZYNi: hopping of V_O and H from the anelastic spectrum

The level of hydration and therefore the concentration of V_O and H is reflected in the anelastic spectra through the amplitudes of the peaks due to hopping of these defects. In BCY and BZ the situation is relatively clear, as that the peaks due to hopping of V_O and H, respectively above and below room temperature at few kHz, can be suppressed almost completely by hydrating or outgassing (Figs. 14, 15). Instead, in BCZYNi the saturation vapour pressure of water is not sufficient to achieve full hydration, neither before nor after exsolution. This is indicated by the presence of the high temperature relaxations due to V_O even when measuring in water saturated conditions (red curve of Fig. 5), and the fact that the maximum hydration weighed after a prolonged anneal in water saturated atmosphere was 0.057 mol H_2O, slightly above 1/3 of the theoretical limit ≥0.15, considering 0.15 Y and that also Ni is an acceptor. A possible mechanism contributing to the reduced hydration capability of BCZYNi will be discussed in Section 4.5.

We did not attempt fits of the anelastic spectra, because in most cases higher frequencies could not be measured and, even when this was done prior to exsolution (Fig. 4), additional difficulties exist. In the as sintered state, peak L1 is prominent and H2 and H3 distinct enough, but comparing the two frequencies it is evident a strong influence of the transition at T_2 on H1 and perhaps also L1. These peaks cannot be fitted in terms of broadened Debye relaxations with amplitude $\propto 1/T$, because of a divergence of the amplitude at T_2. The effect appears similar to that on peak H2 in BCY10 (15) and ascribed to the partial ordering/disordering of V_O [31,33] between the nonequivalent sublattices of the O phase near T_2 [46,52,53], but we do not know how to describe it quantitatively. On the other hand, after outgassing the transition seems suppressed, but all the peaks from L1 to H3 are so overlapped to make any fit very uncertain. The fit would be particularly challenging in the high temperature region, where the contribution of the motion of domain walls in the rhombohedral phase is evident from the step of the Q^{-1} curve below T_1, but its temperature dependence is unknown.

From these anelastic spectra it can be concluded that free and trapped V_O and H in BCZYNi grossly behave similarly to those in $BaZrO_3$ and $BaCe_{1-x}Y_xO_3$, with a separation between the two ranges of activation energies at ~0.5 eV, but we are not able to make reliable assignments of the peaks H1–H3 to V_O that are free and trapped by Y, Ni and possibly V_{Ba} after exsolution. As for H hopping, below room temperature it should be almost completely trapped, so that the intense peak L1 should be due to the most abundant H trapped at Y.

4.4. Analysis of the dielectric spectra

From Fig. 9 it appears that the dielectric spectrum contains a major relaxation process, L1d in the hydrated state and H1d at higher temperature after outgassing. These relaxations are fitted as P1 in Figs. 12 and 13, with activation energy $E_{H1} = 0.51$ eV in the exsolved partially hydrated state and $E_{L1} = 0.84$ eV after outgassing, which seem consistent with H hopping in the first case and V_O hopping in the second. In addition, these peaks are close to single Debye relaxations, an unexpected feature with so much cation disorder, which encourages an effort to better understand their nature. The fitting parameters should however be considered with caution, since constant relaxation strengths Δ are used, whereas the populations of all the defects involving V_O and H will change with temperature.

The most obvious interpretation would be that H1d and L1d are due to the reorientation of Y–V_O and Y–H pairs respectively and, in fact, similar dielectric relaxation peaks have been found in $BaCe_{0.7}Zr_{0.1}Y_{0.2}O_{3-\delta}$ under dry and wet conditions and interpreted in this manner [58]. However, a closer look to their intensity and relaxation time indicates that such a simple explanation cannot hold in our case.

Let us examine the fitted values of the preexponential factor τ_1 and relaxation magnitude Δ_1. The latter is proportional to the probabilities of both the initial and final state, so that, if they differ in energy of A, the thermodynamic factor $1/T$ must be multiplied by $\cosh^{-2}(A/2k_BT)$ [59,60]. Therefore, at $k_BT < A$ relaxation modes like trapping/detrapping are depressed by the asymmetry factor and their intensity increases with increasing T, rather than following the $1/T$ law. In the present fits the asymmetry factor was included but yielded $A \ll k_BT$, so that it is not reported. This means that the majority of relaxation modes connected with asymmetric jumps contribute to a broad background, while L1d and H1d must be due to well defined processes with jumps among energetically equivalent positions, like hopping far from dopants, or around isolated Y atoms. Therefore, the fraction of protons and V_O contributing to P1 is less than their total concentrations. The relaxation magnitude from the reorientation of a molar concentration c of electric dipoles, each causing a change Δp, is [61,62]

$$\Delta = \frac{c\ (\Delta p)^2}{3\varepsilon_0 v_0 k_B}\ , \tag{6}$$

where ε_0 is the permittivity of vacuum and v_0 the molecular volume. To make order of magnitude estimates let us consider a H/V_O trapped at pseudocubic cell containing Y^{3+} and the relaxation mode where it passes from a cube face to the opposite one, with a change of electric dipole $\Delta p_H = ea$, $\Delta p_V = 2ea$. We set $a = 4.39$ Å(pseudocubic cell), $c_V \leq 0.1$ and $c_H \leq 0.042$ from the estimated hydration level of 0.021 mol H_2O after exsolution, where the inequalities mean that not all the H and V_O participate to the P1 relaxation. Using the relaxation strengths Δ_1 in Table 1, we obtain $\Delta_1/\Delta_V \geq 17$ for hopping of $V_O^{\cdot\cdot}$ around Y′ and $\Delta_1/\Delta_H \geq 97$ for hopping of $H^{\cdot}$ around Y′. Even taking into account large uncertainties in the fitting parameters, these estimates exclude simple dipolar relaxations, but rather suggest that the prevailing relaxation mode involves several jumps over a distance l, so that the effective change of dipole is el rather than ea, and $l \geq 4a - 10a$ would account for the observations.

Also the preexponential factors of the relaxation time are too large for dipolar relaxations from single jumps of protons or V_O trapped by acceptors. Their reciprocal τ_1^{-1} should be close to the optical phonon vibration frequency responsible for the jump, which is ~10^{14} Hz for the O–H stretching mode [63], assumed to be relevant in $BaCeO_3$ based perovskites [64], down to 10^{13} Hz in case the jumps are assisted by softer O–B–O bending modes [65] . The discrepancy between τ_1^{-1} and the optical phonon frequencies is within an order of magnitude for V_O, but two orders of magnitude for H hopping. The discrepancy in the latter case can partly or completely be due to the involvement of proton tunnelling, since in that case τ_1^{-1} is not a phonon frequency but a strongly renormalized squared tunnelling matrix element of the proton also in the high temperature Arrhenius-like limit [66–70]. The rotational motion of H/D about O coordinated to Y in $BaCe_{1-x}Y_xO_3$ has been demonstrated to heavily involve tunnelling [30] and, to a lesser extent, tunnelling might assist the longer jumps to a different O atom. Even if this were not the case, there is another mechanism that may

lower the so-called attempt frequency with respect to the promoting local phonon frequency. If the hopping atom is much lighter than the surrounding ones, as H in BCZYNi is, it may not loose its energy in collisions immediately after the jump, as implied by absolute rate theory, and jump back. This reduces the attempt frequency of δ/k_BT, where δ is the average energy lost by the proton in a collision with surrounding atoms [63,71], and δ is expected to be much smaller than the acquired saddle point energy, due to the large difference of masses of the colliding atoms.

Summarizing, both the relaxation magnitudes and preexponential factors of P1 are compatible with hopping over a distance $\gtrsim 4a$. The easiest manner to explain the major peak P1 in the hydrated and outgassed state would be that there is a prevalence of dopant clusters, spanning about 4–10 cells, within which both H and V_O can easily jump. The mechanism is analogous to the Maxwell-Wagner relaxation but, instead of free electronic charges between grain boundaries or electrodes, it would be due to the motion $H^{\cdot}$ and $V_O^{\cdot\cdot}$ within these dopant clusters. The mechanism is also analogous to the nanoscale percolation proposed to determine the proton conductivity in $BaZr_{1-x}Y_xO_3$ [72], though here the focus is on paths that are short rather than percolating through the sample. It is noteworthy that the percolation threshold for the dopant network is 15% Y [73], rendering more convincing that in BCZYNi a considerable fraction of dopants form clusters along 4–10 cells. The additional constraint of nearly single Debye peaks suggests that the relaxations originate in clusters, likely of the most abundant Y dopant, with a distribution of sizes peaked at 5–10 unit cells.

Besides the above mentioned simulations of $BaZr_{1-x}Y_xO_3$ [72–74], additional literature supports both the existance of dopant clusters and local fast hopping within them.

4.4.1. Dopant clusters

We are looking for a relaxation mode where the H/V_O spans $\gtrsim 4$ cells. Therefore, we explore the possibility that short chains of dopants are more stable than purely random distributions at the sintering conditions, where V_O compensate the dopants. These linear clusters of dopants and V_O would be partially stabilized by electrostatic interaction when the cations are mobile and would remain frozen at lower temperatures where only the V_O are mobile. Indeed, the existence of clusters of dopants in oxide ion conductors has been proposed both after first principle calculations and experimental indications.

Defect association energies of dopants and V_O have been calculated for $BaZrO_3$ [75], finding that the dopant pairs have positive energy, dictated more by the mismatch between the size of the dopant and of Zr than electrostatic repulsion. A Y–O–Y pair has an interaction energy of 0.26 eV, but the interaction energy of Y–V_O is −0.45 eV, so that a linear Y–V_O–Y cluster should be favoured in $BaZrO_3$. In $BaCeO_3$ Ce has a size close to Y and the repulsive Y–Y energy should be reduced, making the pair even more favourable, based on this analysis [75]. The existence of stable Y– V_O–Y complexes has been experimentally demonstrated in fluorite type $Ce_{1-x}Y_xO_{2-\delta}$ and $Zr_{1-x}Y_xO_{2-\delta}$, where the anelastic relaxations of V_O hopping about the axis of the Y pair has been measured, and already at $x = 0.18$ these complexes are largely predominant over isolated Y [76,77].

The formation of M–V_O–M where M are trivalent dopants in $BaCeO_3$ has also been studied theoretically more recently [78], finding that they would be predominant for M = In, Sc, with M–V_O association enthalpies of 0.47 and 0.33 eV respectively, but less abundant for M = Y, with a calculated Y–V_O association enthalpy of 0.084 eV (Fig. 5 of [78]).

Triangular clusters of triple Y dopants have been proposed [36] to exist in $BaZr_{0.8}Y_{0.2}O_3$, where they would be strong traps for protons, but such a compact geometry has not been experimentally confirmed and it would not help explaining large effective dipoles. The comparison of such simulations with experimental conductivities confirms anyway that Y association in pairs is predominant over isolated Y.

Linear geometries of next nearest neighbour Y dopants are suggested by DFT calculations for $BaZr_{1-x}Y_xO_3$ with $x = 0.07$, 0.15, 0.22 and 0.3 [73]. At $x = 0.07$ the configuration with lowest energy consists of triplets of Y along the pseudocubic ⟨100⟩ direction, which becomes a stripe along ⟨110⟩ of nearest neighbour Y atoms at $x = 0.22$, close to our doping. If a consistent fraction of dopants were preferentially arranged according to motifs like these, the enhanced dielectric relaxation might be explained by the diffusion of V_O and protons along these networks of dopants without need of detrapping. The mechanism is the same as proposed to explain the dependence of proton conductivity on doping in $BaZr_{1-x}Y_xO_{3-\delta}$, but in that case the focus is on percolating networks for long range diffusion [72,73], while we are considering shorter segments.

For completeness, we mention another model that had originally been proposed for explaining the larger than expected magnitude of dielectric relaxation in fluorite type $Ce_{1-x}Y_xO_{2-\delta}$. It is the "wrong pair" model [79], which however seems more appropriate for low dopant concentrations, well below our case.

4.4.2. Comparison with the anelastic spectra

There is no clear correlation between the anelastic peaks L1 and H1 and the major dielectric peaks L1d and H1d in the partially hydrated and outgassed states. Not only their temperatures but also their relative intensities are different, with L1 but not L1d well visible also in the hydrated state.

The anelastic analogue of the Maxwell-Wagner-like dielectric relaxation proposed above within short clusters is in principle possible. The Gorsky effect is the migration of defects along the sample thickness during flexural vibrations [45], where a non homogeneous compressive stress is generated along the sample thickness, and its magnitude depends on the trace of the elastic dipole of the defects. It has been measured for interstitial H in extremely thin metallic samples [80,81], and it has also been proposed that in recrystallized metallic glasses the H migration would be confined by grain boundaries [82], thereby shortening the relaxation time. In our case, the migration of H and V_O might be driven along the same clusters invoked for dielectric relaxation by the non homogeneous stress acting on their volume mismatch with the lattice. We think, however, that the relaxation strength for such a mechanism is much smaller than that for the usually observed relaxation from the reorientation of their anisotropic elastic dipoles.

4.5. Reduced hydration capability

As explained before, unlike in BCY and BZ, the anelastic relaxations H1–H3 due to V_O are not completely suppressed by hydration. This is in agreement with the mass gain and loss after hydration and outgassing treatments, indicating that the maximum hydration level attainable in BCZYNi is 57% of the theoretical maximum. So reduced a hydration capability is unlike the similar composition $BaCe_{0.7}Zr_{0.1}Y_{0.1}Yb_{0.1}O_{3-\delta}$ where $\delta = 0.1$ in wet air [54] and $BaZr_{0.8-x}Ce_xY_{0.2}O_{3-\delta}$, where 95% hydration is possible for $x > 0.6$ [2].

Possible mechanisms that hinder hydration are the formation of stable dopant complexes, which has been discussed in Section 4.4.1. In that case, the focus was on networks of dopants, not necessarily nearest neighbours, while now we consider pairs of nearest neighbour dopants [78,83]. These pairs should be particularly strong traps for V_O , like Y–V_O–Y and possibly Y–V_O–Ni, and would prevent these V_O from being hydrated. The equilibrium concentration of M–V_O–M complexes, with M = trivalent dopant, in $BaCe_{1-x}M_xO_3$ versus sintering temperature has been calculated as 2–5% mol for $x = 0.1$ [78]. Considering that we have 0.15 Y and 0.05 Ni, or possibly up to 0.05 V_{Ba} after exsolution, this is the right order of magnitude for explaining the reduction of hydration capability we observed in BCZYNi. Notice that B-site vacancies are unlikely to form after exsolution, because the short and strong B–O bonds in ABO_3 perovskites make the formation energy of V_B much higher than that of V_A [84], and a recent theoretical analysis of Ni exsolution in $SrTiO_3$ shows that the fastest diffusion paths of Ni is in association with V_O and V_A [85]). The strong association of

V_O dopant clusters should be present also in BCY10, even though with a lower content of acceptors with respect to BCZYNi; yet in Fig. 15 the major peak H1 due to V_O hopping can be completely eliminated by hydration. The point is that V_O trapped in stable complexes with two acceptors not only do not contribute to the mass change after treatments at relatively low temperatures of this study, but they would also be invisible to the anelastic and dielectric spectroscopies. In fact, such configurations should have a large binding energy and the V_O would not have equivalent sites to jump to, like the six O sites first neighbours to an isolated acceptor. Therefore, the relaxation mode from the jumps out or into such stable configurations would involve a change in initial and final energy equal to E_b and a thermodynamic factor $\cosh^{-2}\left(E_b/k_BT\right)$ which reduces the relaxation strength [59,60].

Summarizing, at concentrations as high as ≥0.15 the dopants cannot be considered as randomly distributed and isolated, but their actual distribution, determined by the sintering conditions, affects the hydration capacity and ionic mobilities. We propose that at ≥0.15 the majority of dopants is not isolated but aggregated in essentially two types of clusters: (1) isolated nearest neighbour Y–O–Y pairs and (2) longer nearly 1D clusters, possibly looser than straight Y–O–Y–O–Y– chains, where the Y dopants are mainly second Nearest Neighbours (NN). The isolated pairs would effectively trap V_O, forming particularly stable Y– V_O–Y complexes, that make them unavailable to hydration and invisible to anelastic and dielectric spectroscopies, partially accounting for the reduced hydration capability of strongly doped BCZYNi. The longer clusters would act as paths for fast diffusion of H and V_O without need of detrapping.

The spacial distribution of dopants is determined by the sintering conditions, since higher temperature and longer time yield more uniform and dispersed distributions of dopants. An important indication of the possibility of controlling the concentration of NN pairs of dopants has been given by varying the sintering temperature of $BaCe_{0.9}In_{0.1}O_{3-\delta}$ from 1300 °C to 1600 °C, finding that the maximum hydration level passes from ≃0.08 to ≃0.1 [78].

A variant of the above picture is suggested by a recent study of $BaZr_{0.8}$ $Yb_{0.2}O_3$ with additional 2–5% Ni [86], where STEM high-angle annular dark field imaging reveals clusters of Yb and Ni. It is therefore proposed that Ni–Yb pairs trap V_O with a calculated binding energy of 0.92 eV and considerably reduce their hydration enthalpy. We may apply also to our case the notion that Ni preferentially clusters with Y and the Y–V_O–Ni complexes are the main reason for the reduced hydration. Then, since no evident increase of hydration is found after exsolution, we should also suppose that most Ni leaves a Ba vacancy [85], which takes the role of the strong trapping centre, possibly together with Y, for V_O.

There is an additional phenomenon related to the distribution of acceptor dopants in perovskite but also fluorite proton conductors: their segregation to the grain boundaries to neutralize the charge from V_O during high temperature sintering or annealing [87]. We have no indications of segregation of Y at grain boundaries in BCZYNi, which would not significantly reduce the concentration of Y in the bulk anyway, since in BCZY it is found limited to the first atomic plane at the grain boundary [88]. The presence of an atomic layer enriched with Y at the grain boundaries would therefore have little effect on the anelastic spectra and the low temperature dielectric relaxations, which probe the bulk.

4.6. Structural phase transitions

The phase transitions revealed by the anomalies in the elastic modulus at T_1 and T_2 can be recognized as octahedral tilt transitions, by comparison with the archetypal $BaCeO_3$ and other compositions more similar to the present one. The sequence of transitions in $BaCeO_3$ is, starting from high temperature: cubic $Pm\bar{3}m$ (C), rhombohedral $R\bar{3}c$ (R), orthorhombic Imma (O), orthorhombic $Pnma$ (O′) [53–55]. Accordingly, the phase transitions appearing as elastic anomalies in $BaCe_{1-x}Y_xO_3$ have been assigned as $C \overset{T_1}{\rightarrow} R \overset{T_2}{\rightarrow} O \overset{T_3}{\rightarrow} O'$ [33].

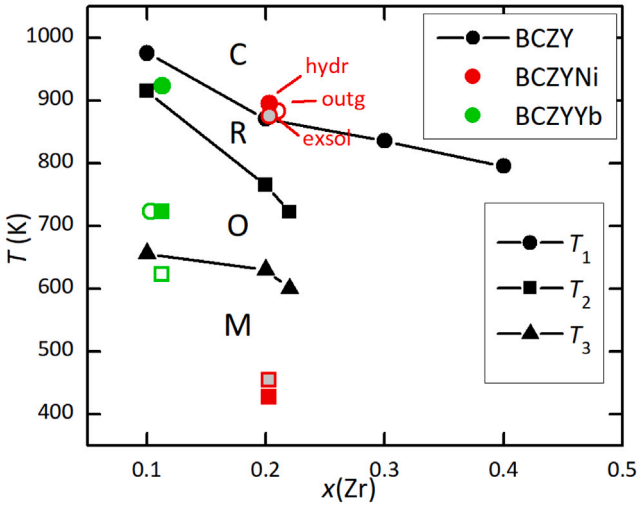

Fig. 16. Transition temperatures T_1 and T_2 from the anelastic spectra (red), with the size of symbols approximately representing the uncertainty in T, plotted in the phase diagram of $BaCe_{0.85-x}Zr_xY_{0.15}O_{3-\delta}$ from Ref. [90] (black) at x chosen to match the tolerance factors. The green symbols are for $BaCe_{0.7}Zr_{0.1}Y_{0.1}Yb_{0.1}O_{3-\delta}$ [91].

From Fig. 4 it is clear that above T_1 the phase is cubic: the drop of Q^{-1} indicates the vanishing of the domain walls and the large step in the modulus is what is expected from a phase transition where the order parameter is quadratically coupled to strain, as is the case of the octahedral tilt angle, and is null in the high temperature phase [89]. The anomalies in the elastic modulus are also similar to those in $BaCeO_3$, where a negative step is found passing from C to the R phase, while minima signal further changes of the tilt patterns.

The transition temperatures in BCZYNi are plotted as red symbols in the phase diagram of $BaCe_{0.85-x}Zr_xY_{0.15}O_{3-\delta}$ [90] (black symbols in Fig. 16). The composition was chosen in order to match the tolerance factors, Eq. (5). Assuming $\delta = 0$ instead of the estimated ~0.03 [90], $BaCe_{0.85-x}Zr_xY_{0.15}O_3$ at $x = 0.203$ has the same $t = 0.954$ of our $BaCe_{0.7}Zr_{0.1}Y_{0.15}Ni_{0.05}O_3$. Indeed, in this manner T_1 of the two compositions nearly overalp, but the same cannot be said for T_2 and for the effect of V_O on these temperatures. BCZYNi does not behave as explained in Section 4.2 for BCY: based on the fact that T_2 decreases of 200–300 K in $BaCe_{1-x}Y_xO_3$ with $x = 0.1$–0.2 after outgassing, we would expect that also in BCZYNi T_2 shifts downwards of at least 100 K after outgassing. Instead, the minimum of the intermediate green curve of Fig. 7 seems depressed in amplitude rather than in T_2, the shifted being of only ~10 K. With further outgassing, the residual anomaly at the same temperature might be accounted for by the modulus defect of relaxation H1, suggesting the disappearance of the transition rather than its shift to lower temperature.

Little can be said on the dependence of T_1 on the hydration level, because hydration is either very low or fast decreasing during the anelastic measurement in vacuum. It seems, however, that the exsolution treatment depressed T_1 of ~15 K in both the fully (Fig. 5) and partially outgassed states, suggesting that the exsolution created defects. Most likely, the migration of Ni was not accompanied by an equal loss of BaO, but left V_{Ba} in the bulk. In fact, if the loss of BaO fully compensated the loss of Ni from the bulk, the new stoichiometries would be 0 for Ni and divided by 0.95 for Ce, Zr and Y. If so, the tolerance factor would pass from 0.954 to 0.948, implying an enhancement of the lattice mismatch and hence of T_1. The decrease of T_1 indicates that defects, presumably V_{Ba}, where created in the bulk.

For completeness, in Fig. 16 are also plotted the transition temperatures of $BaCe_{0.7}Zr_{0.1}Y_{0.1}Yb_{0.1}O_{3-\delta}$ (BCZYYb7111) from XRD [91], which is close to our composition and much studied. They are plotted

as green symbols with the same criterion used for BCZYNi, of matching the tolerance factor of BCZY. In that study the usual sequence of phases C/R/O is reported, and also a marked decrease of both T_1 and T_2 with V_O (closed/open symbols in wet/dry condition), as observed in BCY. It appears that, though the onset of the first tilt transition from the cubic state is mainly determined by be the tolerance factor, the subsequent transitions depend in a more complicate manner on the composition. Actually, there is an ongoing debate on the nature of the polymorphic transitions in BCZYYb7111, with studies that differ not only in the transition temperatures, but also in their number and in the various phases, as summarized in Ref. [54]. So, the room temperature phase is generally identified as O, but it may also be M or R. The most recent study combining XRD and neutron diffraction (though with different p_{H_2O}) even indicates only one transition at 923 K to the $I4/mcm$ tetragonal phase [54], but it must be said that the reported temperature dependence of the lattice parameters suggests a second transition around 773 K. Among the causes of discordance in assigning the phases, are pointed out the scarce sensitivity of XRD to O and hence to octahedral tilting, and differences in p_{H_2O} [54,91], but we suggest that also the cation distribution and various defects, depending on the preparation route, have a role.

An additional phase transition is indicated by the dielectric anomaly at T_3 (Fig. 9) but is completely absent in the anelastic spectra. This makes a change in the octahedral tilt pattern a very unlikely explanation, since in that case the anomaly should be evident in the anelastic rather than dielectric spectra. In fact, an octahedral tilt transition is improper ferroelastic and therefore gives a clear signature in some of the elastic constants: a step-like softening below the transition temperature. The effect of the same transition on the dielectric permittivity can be a minor step, if tilting is coupled to polarization, as it occurs for a recently discovered transition in PZT [92,93]. The large thermal hysteresis and near absence of the anomaly during cooling suggests some sort of ordering of charged defects, as V_O and H are, with concomitant change in the electronic structure, but we could not find similar anomalies in the literature on perovksite proton conductors. It would certainly be worth further studying the nature of this new phase transition.

5. Conclusions

We measured the anelastic and dielectric susceptibilities of BCZYNi under dry and wet conditions before and after Ni exsolution, and compared with anelastic spectra measured under similar conditions in unintentionally doped $BaZrO_3$ and BCY10. The anelastic spectra contain the relaxation peaks above room temperature due to hopping of V_O also in wet conditions, indicating that hydration is incomplete. This is confirmed by observing that the maximum uptake of H_2O under usual wet conditions is 57% of the theoretical limit of 0.1 mol.

Major relaxation processes, close to single Debye, are found in the dielectric spectrum, whose activation energies are 0.51 eV in the partially hydrate state and 0.84 eV in the outgassed state. If they are interpreted in terms of hopping of H in the first case and V_O in the second, their large amplitude and long relaxation time exclude simple dipolar relaxations of Y–H and Y–V_O pairs, and indicate relaxation modes where H and V_O span several lattice cells. The possibility is discussed that a consistent fraction of dopants is arranged into almost linear clusters within which H and V_O can diffuse without need of detrapping, similarly to the nanoscale percolation proposed to explain the proton conductivity of $BaZr_{1-x}Y_xO_{3-\delta}$ [72].

At high doping levels, ≥10%, the spacial distribution of dopants can determine the hydration capability and proton conductivity in possibly contrasting manners. On the one hand, isolated pairs of NN dopants act as strong traps for V_O, reducing their mobility and availability to be hydrated; on the other hand, longer and possibly looser aggregates of dopants may act as preferential diffusion paths for protons and V_O without detrapping.

Steps and minima in the Young's moduls occur at two octahedral tilt transitions at T_1 = 860–900 K and T_2 ~ 450 K, while a step in the dielectric susceptibility at ~260 K reveals a new phase transition. The latter does not seem to be a third tilt transition, as in $BaCeO_3$, because it is not accompanied by an elastic anomaly. The temperatures of the tilt transitions are compared with those of similar materials. While T_1 is mainly determined by the average B cation size and tolerance factor, the behaviour of T_2 is much more difficult to understand and apparently depends on the composition and arrangement of the B cations in materials with multiple cation substitutions.

CRediT authorship contribution statement

Francesco Cordero: Writing – review & editing, Writing – original draft, Investigation, Data curation. **Floriana Craciun:** Writing – review & editing, Investigation. **Andrea Brigliadori:** Writing – original draft, Methodology, Investigation. **Andrea Bartoletti:** Writing – review & editing, Methodology, Investigation. **Matteo Ardit:** Writing – original draft, Investigation. **Pietro Galizia:** Writing – review & editing, Project administration, Methodology, Investigation, Funding acquisition. **Angela Gondolini:** Project administration, Methodology, Conceptualization. **Elisa Mercadelli:** Writing – review & editing, Project administration, Methodology, Conceptualization. **Alessandra Sanson:** Supervision, Project administration, Funding acquisition.

Declaration of competing interest

The authors declare that they have no known competing financial interests or personal relationships that could have appeared to influence the work reported in this paper.

Acknowledgements

This work has been partially funded by (i) European Union – NextGenerationEU– Project SELWA – CUP B53D23008660006 - Grant Assignment Decree No 20229PNWM7, (ii) the European Union – NextGeneration EU from the Italian Ministry of Environment and Energy Security POR H2 AdP MMES/ENEA with involvement of CNR and RSE, PNRR - Mission 2, Component 2, Investment 3.5 "Ricerca e sviluppo sull'idrogeno", CUP: B93C22000630006 and (iii) by the agreement between Italian Ministry for the Environment and Energy Security and the Italian National Research Council "Ricerca di Sistema Elettrico Nazionale", in the frame of the project "Frontier materials for energy applications".

AS and AB acknowledge Project code PE0000021, Concession Decree No. 1561 of 11.10.2022 adopted by Ministero dell'Universitá e della Ricerca (MUR),CUP B53C22004060006, Project title "Network 4 Energy Sustainable Transition—NEST", funded by the National Recovery and Resilience Plan (NRRP), Mission 4 Component 2 Investment 1.3—Call for tender No. 1561 of 11.10.2022 of Ministero dell'Universitá e della Ricerca (MUR), funded by the European Union—NextGenerationEU. FC and FC acknowledge the precious technical assistance of M.P. Latino (CNR-ISM). Mr. Cesare Melandri is gratefully acknowledged for the precision cutting of the specimens.

References

[1] M. Chen, M. Zhou, Z. Liu, J. Liu, A comparative investigation on protonic ceramic fuel cell electrolytes $BaZr_{0.8}Y_{0.2}O_{3-\delta}$ and $BaZr_{0.1}Ce_{0.7}Y_{0.2}O_{3-\delta}$ with NiO as sintering aid, Ceram. Int. 48 (2022) 17208, http://dx.doi.org/10.1016/j.ceramint.2022.02.278.

[2] D. Han, X. Liu, T.S. Bjorheim, T. Uda, Yttrium-doped barium zirconate-cerate solid solution as proton conducting electrolyte: Why higher cerium concentration leads to better performance for fuel cells and electrolysis cells, Adv. Energy Mater. 11 (2021) 2003149, http://dx.doi.org/10.1002/aenm.202003149.

[3] Z. Wu, Y. Zhang, Z. Liu, H. Ma, X. Jin, G. Yang, Y. Shi, Z. Shao, S. Li, Rapid gas-phase synthesis of the perovskite-type $BaCe_{0.7}Zr_{0.1}Y_{0.1}Yb_{0.1}O_{3-\delta}$ proton-conducting nanocrystalline electrolyte for intermediate-temperature solid oxide fuel cells, ACS Appl. Mater. Interfaces 14 (2022) 47568, http://dx.doi.org/10.1021/acsami.2c11492.

[4] M.F. Anwar, Y. Yu, M. Khalid, A. Nazar, B. Bibi, M.F. Sarfraz, Zhu, Bin, J. Huang, M.I. Asghar, Electrochemical insights into performance enhancement of protonic ceramic fuel cells with Ba(Zr,Ce,Y)$O_{3-\delta}$ electrolyte, Energy Mater. 5 (2025) 500102, http://dx.doi.org/10.20517/energymater.2025.16.

[5] A. Bartoletti, E. Mercadelli, A. Gondolini, V. Saraceni, A. Fasolini, J.D. Maron, F. Basile, A. Sanson, Nanostructured ceramic membranes for hydrogen separation, Sep. Purif. Technol. 372 (2025) 133436, http://dx.doi.org/10.1016/j.seppur.2025.133436.

[6] A. Bartoletti, E. Mercadelli, V. Saraceni, A. Sangiorgi, A. Gondolini, C. Melandri, P. Pinasco, P. Gramazio, A. Fasolini, J.D. Maron, F. Basile, A. Sanson, 3D-printed ceramic membranes: Fabrication and hydrogen permeation performance, J. Membr. Sci. 733 (2025) 124311, http://dx.doi.org/10.1016/j.memsci.2025.124311.

[7] E. Mercadelli, A. Gondolini, M. Ardit, G. Cruciani, C. Melandri, S. Escoláástico, J.M. Serra, A. Sanson, Chemical and mechanical stability of BCZY-GDC membranes for hydrogen separation, Sep. Purif. Technol. 289 (2022) 120795, http://dx.doi.org/10.1016/j.seppur.2022.120795.

[8] F. Bagioni, E. Mercadelli, A. Bartoletti, P. Pinasco, M. Ardit, N. Precisvalle, S. Massardo, S. Presto, M. Viviani, A. Gondolini, A. Sanson, Synthesis strategies for $BaCe_{0.7}Zr_{0.1}Y_{0.1}Yb_{0.1}O_{3-\delta}$ for the development of high-conducting solid oxide cell electrolyte, Int. J. Hydrog. Energy 193 (2025) 152384, http://dx.doi.org/10.1016/j.ijhydene.2025.152384.

[9] H. Guo, Y. Li, L. Jiang, Y. Sha, S. Guo, D. Han, Transport properties of the Ba(Zr, Ce, Y, Yb)$O_{3-\delta}$ proton conductor: the real role of co-substitution of Y and Yb, J. Mater. Chem. A 12 (2024) 5875, http://dx.doi.org/10.1039/d3ta07486b.

[10] Y.D. Kim, I.H. Kim, C. Meisel, C. Herradón, P.W. Rand, J. Yang, H.S. Kim, N.P. Sullivan, R. O'Hayre, Improving tubular protonic ceramic fuel cell performance by compensating Ba evaporation via a Ba-excess optimized proton conducting electrolyte synthesis strategy, J. Phys. Energy 6 (2024) http://dx.doi.org/10.1088/2515-7655/ad5760.

[11] A.J.E. Rowberg, M.W. Swift, C.G.V. de Walle, Understanding carbon contamination in the proton-conducting zirconates and cerates, Phys. Chem. Chem. Phys. 23 (2021) 14205, http://dx.doi.org/10.1039/D1CP01902C.

[12] N.A. Danilov, I.A. Starostina, G.N. Starostin, A.V. Kasyanova, D.A. Medvedev, Z. Shao, Fundamental understanding and applications of protonic Y- and Yb-coped Ba(Ce,Zr)O_3 perovskites: State-of-the-art and perspectives, Adv. Energy Mater. 13 (2023) 2302175, http://dx.doi.org/10.1002/aenm.202302175.

[13] M.K. Hossain, R.C. Das, M.I. Hossain, M.A. Rahman, P. Paramasivam, R. Chakma, M. Amami, M.H. Mahmoud, R. Bousbih, R. Haldhar, K. Hashizume, Prospects and challenges of proton conducting cerates in electrochemical hydrogen devices for clean energy systems: A review, Glob. Challenges 9 (2025) e00119, http://dx.doi.org/10.1002/gch2.202500119.

[14] C.Y.R. Vera, H. Ding, D. Peterson, W.T. Gibbons, M. Zhou, D. Ding, A mini-review on proton conduction of BaZrO3- based perovskite electrolytes, J. Phys. Energy 3 (2021) 032019, http://dx.doi.org/10.1088/2515-7655/ac12ab.

[15] M.K. Hossain, R. Chanda, A. El-Denglawey, T. Emrose, M.T. Rahman, M.C. Biswas, K. Hashizume, Recent progress in barium zirconate proton conductors for electrochemical hydrogen device applications: A review, Ceram. Int. 47 (2021) 23725, http://dx.doi.org/10.1016/j.ceramint.2021.05.167.

[16] S. Jeong, T. Kobayashi, K. Kuroda, H. Kwon, C. Zhu, H. Habazaki, Y. Aoki, Evaluation of thin film fuel cells with Zr-rich BaZr: $XCe_{0.8-x}Y_{0.2}O_{3-\delta}$ electrolytes ($x \geq 0.4$) fabricated by a single-step reactive sintering method, RSC Adv. 8 (2018) 26309, http://dx.doi.org/10.1039/C8RA04724C.

[17] M. Wang, E.I. Papaioannou, I.S. Metcalfe, A. Naden, C.D. Savaniu, J.T. Irvine, The exsolution of Cu particles from doped barium cerate zirconate via barium cuprate intermediate phases, Adv. Func. Mater. 33 (2023) 2302102, http://dx.doi.org/10.1002/adfm.202302102.

[18] D. Neagu, E.I. Papaioannou, W.K.W. Ramli, D.N. Miller, B.J. Murdoch, H. Ménard, A. Umar, A.J. Barlow, P.J. Cumpson, J.T.S. Irvine, I.S. Metcalfe, Demonstration of chemistry at a point through restructuring and catalytic activation at anchored nanoparticles, Nat. Commun. 8 (2017) 1855, http://dx.doi.org/10.1038/s41467-017-01880-y.

[19] M.L. Weber, M. Wilhelm, L. Jin, U. Breuer, R. Dittmann, R. Waser, O. Guillon, C. Lenser, F. Gunkel, Exsolution of embedded nanoparticles in defect engineered perovskite layers, ACS Nano 15 (2021) 4546, http://dx.doi.org/10.1021/acsnano.0c08657.

[20] A.J. Carrillo, K.J. Kim, Z.D. Hood, A.H. Bork, J.L. Rupp, $La_{0.6}Sr_{0.4}Cr_{0.8}Co_{0.2}O_3$ perovskite decorated with exsolved Co nanoparticles for stable CO_2 splitting and syngas production, ACS Appl. Energy Mater. 3 (2020) 4569, http://dx.doi.org/10.1021/acsaem.0c00249.

[21] A. López-García, L. Almar, S. Escolástico, A.B. Hungría, A.J. Carrillo, J.M. Serra, Tuning ternary alloyed nanoparticle composition and morphology by exsolution in double perovskite electrodes for CO_2 electrolysis, ACS Appl. Energy Mater. 5 (2022) 13269, http://dx.doi.org/10.1021/acsaem.2c01829.

[22] M. Marasi, A.P. Panunzi, L. Duranti, N. Lisi, Di Elisabetta Bartolomeo, Enhancing oxygen reduction activity and structural stability of $La_{0.6}Sr_{0.4}FeO_{3-\delta}$ by 1 mol % Pt and Ru, B-site doping for application in all-perovskite IT-SOFCs, ACS Appl. Energy Mater. 5 (2022) 2918, http://dx.doi.org/10.1021/acsaem.1c03613.

[23] M. Kothari, Y. Jeon, D.N. Miller, A. Eva Pascui, J. Kilmartin, D. Wails, S. Ramos, A. Chadwick, J.T.S. Irvine, Platinum incorporation into titanate perovskites to deliver emergent active and stable platinum nanoparticles, Nat. Chem. 13 (2021) 677, http://dx.doi.org/10.1038/s41557-021-00696-0.

[24] D. Neagu, J.T.S. Irvine, J. Wang, B. Yildiz, A.K. Opitz, J. Fleig, Y. Wang, J. Liu, L. Shen, F. Ciucci, B.A. Rosen, Y. Xiao, K. Xie, G. Yang, Z. Shao, Y. Zhang, J. Reinke, T.A. Schmauss, S.A. Barnett, R. Maring, V. Kyriakou, U. Mushtaq, M.N. Tsampas, Y. Kim, R. Ohayre, A.J. Carrillo, T. Ruh, L. Lindenthal, F. Schrenk, C. Rameshan, E.I. Papaioannou, K. Kousi, I.S. Metcalfe, X. Xu, G. Liu, Roadmap on exsolution for energy applications, J. Phys. : Energy 5 (2023) 031501, http://dx.doi.org/10.1088/2515-7655/acd146.

[25] T. Nakamura, S. Mizunuma, Y. Kimura, Y. Mikami, K. Yamauchi, T. Kuroha, N. Taniguchi, Y. Tsuji, Y. Okuyama, K. Amezawa, Energy efficiency of ionic transport through proton conducting ceramic electrolytes for energy conversion applications, J. Mater. Chem. A 6 (2018) 15771, http://dx.doi.org/10.1039/c8ta05373a.

[26] C. Duan, J. Huang, N. Sullivan, R. O'Hayre, Proton-conducting oxides for energy conversion and storage, Appl. Phys. Rev. 7 (2020) 112084, http://dx.doi.org/10.1063/1.5135319.

[27] R. Qiu, F. Zheng, L. Dong, H. Su, C. Wang, B. Liang, J. Liu, J. Huang, J. Zhang, J. Xu, Z. Tao, J. Xue, L. Lei, Revealing the conduction behaviors of $BaCe_xZr_{0.8-x}Y_{0.2}O_{3-\delta}$ by clicking mouse: From experimental and theoretical studies to software development, Adv. Func. Mater. 35 (2025) 2508318, http://dx.doi.org/10.1002/adfm.202508318.

[28] H. Zhu, S. Ricote, R.J. Kee, Faradaic efficiency in protonic-ceramic electrolysis cells, J. Phys. Energy 4 (2022) 014002, http://dx.doi.org/10.1088/2515-7655/ac3729.

[29] S. Bausch, H.G. Bohn, W. Schilling, Anelastic and dielectric relaxation measurements in the protonic conductor Ba3(Ca1.18Nb1.82)O9-d, Solid State Ion. 97 (1997) 517.

[30] F. Cordero, F. Craciun, F. Deganello, V.L. Parola, E. Roncari, A. Sanson, Hydrogen tunneling in the perovskite ionic conductor $BaCe_{1-x}Y_xO_{3-\delta}$, Phys. Rev. B 78 (2008) 054108.

[31] F. Cordero, F. Craciun, F. Trequattrini, Ionic mobility and phase transitions in perovskite oxides for energy applications, Challenges 8 (2017) 5, http://dx.doi.org/10.3390/challe8010005.

[32] F. Cordero, F. Trequattrini, F. Deganello, V.L. Parola, E. Roncari, A. Sanson, Effect of O vacancies on the Young's modulus of the $BaCe_{1-x}Y_xO_{3-\delta}$ perovskite, Appl. Phys. Lett. 94 (2009) 181905.

[33] F. Cordero, F. Trequattrini, F. Deganello, V.L. Parola, E. Roncari, A. Sanson, Effect of doping and oxygen vacancies on the octahedral tilt transitions in the $BaCeO_3$ perovskite, Phys. Rev. B 82 (2010) 104102, http://dx.doi.org/10.1103/PhysRevB.82.104102.

[34] Y. Yamazaki, A. Kuwabara, J. Hyodo, Y. Okuyama, C.A.J. Fisher, S.M. Haile, Oxygen affinity: The missing link enabling prediction of proton conductivities in doped barium zirconates, Chem. Mater. 32 (2020) 7292, http://dx.doi.org/10.1021/acs.chemmater.0c01869.

[35] E. Makagon, O. Kraynis, R. Merkle, J. Maier, I. Lubomirsky, Non-classical electrostriction in hydrated acceptor doped BaZrO3: Proton trapping and dopant size effect, Adv. Funct. Mater. (2021) 2104188, http://dx.doi.org/10.1002/adfm.202104188.

[36] K. Toyoura, W. Meng, D. Han, T. Uda, Preferential proton conduction along a three-dimensional dopant network in yttrium-doped barium zirconate: a first-principles study, J. Mater. Chem. A 6 (2018) 22721, http://dx.doi.org/10.1039/C8TA08283A.

[37] T. Chen, Y. Jing, L.O. Anderson, K. Leonard, H. Matsumoto, N. Aluru, N.H. Perry, Toward durable protonic ceramic cells: Hydration-induced chemical expansion correlates with symmetry in the Y-doped BaZrO3-BaCeO3 solid solution, J. Phys. Chem. C 125 (2021) 26216, http://dx.doi.org/10.1021/acs.jpcc.1c08334.

[38] C.Y.R. Vera, H. Ding, J. Urban-Klaehn, M. Li, Z. Zhao, F. Stewart, H. Tian, X. Liu, Y. Dong, J. Li, M. Zhou, H. Luo, D. Ding, Improving proton conductivity by navigating proton trapping in high scandium-doped barium zirconate electrolytes, Chem. Mater. 35 (2023) 5341, http://dx.doi.org/10.1021/acs.chemmater.3c00531.

[39] T. Wang, Q. Li, X. Liu, M. Bilal, D. Dong, H. Wang, Nanofabrication technologies for low-temperature solid oxide cells: a comprehensive review of techniques, and future challenges perspectives, Energy Rev. 4 (2025) 100163, http://dx.doi.org/10.1016/j.enrev.2025.100163.

[40] F. Hu, B. Wei, B. He, X. Yu, S. Zhao, Y. Chen, W. Wang, L. Zhao, Q. Chen, Recent advances and future prospects in exsolution technology for solid oxide cells, Energy Rev. 4 (2025) 100141, http://dx.doi.org/10.1016/j.enrev.2025.100141.

[41] S. Barison, M. Battagliarin, T. Cavallin, S. Daolio, L. Doubova, M. Fabrizio, S. Boldrini C. Mortaló, R. Gerbasi, Barium non-stoichiometry role on the properties of $Ba_{1+x}Ce_{0.65}Zr_{0.2}0Y_{0.15}O_{3-\delta}$ proton conductors for IT-SOFCs, Fuel Cells 8 (2008) 360, http://dx.doi.org/10.1002/fuce.200800021.

[42] P. Galizia, A. Tavolaro, C. Baldisserri, F. Craciun, E. Mercadelli, Breakthroughs in scanning electron microscopy poling of massive dense, Scr. Mater. 266 (2025) 116795, http://dx.doi.org/10.1016/j.scriptamat.2025.116795.

[43] D. Montaleone, E. Mercadelli, A. Gondolini, M. Ardit, P. Pinasco, A. Sanson, Role of the sintering atmosphere in the densification and phase composition of asymmetric BCZY-GDC composite membrane, J. Eur. Ceram. Soc. 39 (2019) 21, http://dx.doi.org/10.1016/j.jeurceramsoc.2018.01.043.

[44] F. Cordero, L. Dalla Bella, F. Corvasce, P.M. Latino, A. Morbidini, An insert for anelastic spectroscopy measurements from 80 K to 1100 K, Meas. Sci. Technol. 20 (2009) 015702, http://dx.doi.org/10.1088/0957-0233/20/1/015702.

[45] A.S. Nowick, B.S. Berry, Anelastic Relaxation in Crystalline Solids, Academic Press, New York, 1972.

[46] L. Malavasi, C. Ritter, G. Chiodelli, Correlation between thermal properties, electrical conductivity, and crystal structure in the $BaCe_{0.80}Y_{0.20}O_{2.9}$ proton conductor, Chem. Mater. 20 (2008) 2343, http://dx.doi.org/10.1021/cm7033917.

[47] E. Vera, V. Trillaud, J. Metaouaa, M. Aouine, A. Boreave, L. Burel, I.-L. Roiban, P. Steyer, P. Vernoux, Comparative study of exsolved and impregnated Ni nanoparticles supported on nanoporous perovskites for low-temperature CO oxidation, ACS Appl. Mater. Interfaces 16 (2024) 7219, http://dx.doi.org/10.1021/acsami.3c17300.

[48] X. Cao, L. Ke, K. Zhao, X. Yan, X. Wu, N. Yan, Surface decomposition of doped $PrBaMn_2O_{5+\delta}$ induced by in situ nanoparticle exsolution: Quantitative characterization and catalytic effect in methane dry reforming reaction, Chem. Mater. 23 (2022) 10484, http://dx.doi.org/10.1021/acs.chemmater.2c02488.

[49] T. Pagnier, I. Charrier-Cougoulic, C. Ritter, G. Lucazeau, A neutron di raction study of $BaCe_xZr_{1-x}O_3$, Eur. Phys. J. 9 (2000) 1, http://dx.doi.org/10.1051/epjap:2000192.

[50] A.K. Jonscher, Dielectric relaxation in solids, J. Phys. D: Appl. Phys. 32 (1999) R57–R70.

[51] O. Kamishima, Y. Abe, T. Ishii, J. Kawamura, T. Hattori, Dielectric relaxation in Yb-doped $SrZrO_3$, J. Phys. : Condens. Matter 16 (2004) 4971.

[52] K.S. Knight, Structural phase transitions in $BaCeO_3$, Solid State Ion. 74 (1994) 109.

[53] K.S. Knight, Structural phase transitions, oxygen vacancy ordering and protonation in doped $BaCeO_3$: results from time-of-flight neutron powder diffraction investigations, Solid State Ion. 145 (2001) 275–294.

[54] L. Hamze, E. Suard, O. Joubert, E. Quarez, Synthesis and temperature dependence of the crystal structure of proton conductor $BaZr_{0.1}Ce_{0.7}Y_{0.1}Yb_{0.1}O_{3-d}$ (BZCYYb1711) by combined neutron and X-ray diffraction, Solid State Ion. 116682 (2024) 116682, http://dx.doi.org/10.1016/j.ssi.2024.116682.

[55] A.K.E. Andersson, S.M. Selbach, T. Grande, C.S. Knee, Thermal evolution of the crystal structure of proton conducting $BaCe_{0.8}Y_{0.2}O_{3-d}$ from high-resolution neutron diffraction in dry and humid atmosphere, Dalton Trans. 44 (2015) 10834, http://dx.doi.org/10.1039/C4DT03948C.

[56] J.B. Goodenough, Electronic and ionic transport properties and other physical aspects of perovskites, Rep. Progr. Phys. 67 (2004) 1915–1993.

[57] R.D. Shannon, C.T. Prewitt, Effective ionic radii in oxides and fluorides, Acta Cryst. B 25 (1969) 925.

[58] S.A. Suhaib, A.K. Zhu, J. Sun, Y.M. Guo, S.T. Wang, C.C. Wang, High-temperature dielectric relaxations in (Ce, Y) codoped $BaZrO_3$ ceramics, Mater. Res. Express 6 (2019) 075010, http://dx.doi.org/10.1088/2053-1591/ab10be.

[59] A.S. Nowick, Partial relaxation magnitudes for anelastic and dielectric relaxation due to point defects, J. Phys. Chem. Sol. 34 (1970) 1507–1521.

[60] F. Cordero, Anelastic (dielectric) relaxation of point defects at any concentration, with blocking effects and formation of complexes, Phys. Rev. B 47 (1993) 7674, http://dx.doi.org/10.1103/PhysRevB.47.7674.

[61] A.S. Nowick, W.R. Heller, Dielectric and anelastic relaxation of crystals containing point defects, Adv. Phys. 14 (1965) 101–166.

[62] I. Kuskovsky, B.S. Lim, A.S. Nowick, Low-temperature dielectric relaxation peaks involving proton tunneling in $Ba_{1-x}Nd_xCeO_3$, Phys. Rev. B 60 (1999) R3713.

[63] A.S. Nowick, Y. Du, High-temperature protonic conductors with perovskite-related structures, Solid State Ion. 77 (1995) 137–146.

[64] P.A. Burr, M.W.D. Cooper, Importance of elastic finite-size effects: Neutral defects in ionic compounds, Phys. Rev. B 96 (2017) 094107, http://dx.doi.org/10.1103/PhysRevB.96.094107.

[65] K.D. Kreuer, A. Fuchs, J. Maier, HD isotope effect of proton conductivity and proton conduction mechanism in oxides, Solid State Ion. 77 (1995) 157, http://dx.doi.org/10.1016/0167-2738(94)00265-T.

[66] P.G. Sundell, M.E. Björketun, G. Wahnström, Density-functional calculations of prefactors and activation energies for H diffusion in $BaZrO_3$, Phys. Rev. B 76 (2007) 094301.

[67] A. Braun, Q. Chen, Experimental neutron scattering evidence for proton polaron in hydrated metal oxide proton conductors, Nat. Commun. 8 (2017) 15830, http://dx.doi.org/10.1038/ncomms15830.

[68] A.L. Samgin, A.N. Ezin, Comment on "proton transport in barium stannate: classical, semi-classical and quantum regimes", Phys. Chem. Chem. Phys. 19 (2017) 21185, http://dx.doi.org/10.1039/c6cp06763h.

[69] J. Ding, J. Balachandran, X. Sang, G.M. Veith, C.A. Bridges, W. Guo, J.S. Anchell, Y. Cheng, C.M. Rouleau, J.D. Poplawsky, N. Bassiri-Gharb, R.R. Unocic, P. Ganesh, The influence of local distortions on proton mobility in acceptor doped perovskites, Chem. Mater. 30 (2018) 4919, http://dx.doi.org/10.1021/acs.chemmater.8b00502.

[70] G. Geneste, Proton transfer in barium zirconate: Lattice reorganization, Landau–Zener curve-crossing approach, Sol. State Ion. 323 (2018) 172, http://dx.doi.org/10.1016/j.ssi.2018.04.017.

[71] A.S. Nowick, A.V. Vaysleyb, Isotope effect and proton hopping in high-temperature protonic conductors, Solid State Ion. 97 (1997) 17.

[72] F.M. Draber, C. Ader, J.P. Arnold, S. Eisele, S. Grieshammer, S. Yamaguchi, M. Martin, Nanoscale percolation in doped $BaZrO_3$ for high proton mobility, Nat. Mater. 19 (2020) 338, http://dx.doi.org/10.1038/s41563-019-0561-7.

[73] S. Kasamatsu, O. Sugino, T. Ogawa, A. Kuwabara, Dopant arrangements in Y-doped $BaZrO_3$ under processing conditions and their impact on proton conduction: a large-scale first-principles thermodynamics study, J. Mater. Chem. A 8 (2020) 12674, http://dx.doi.org/10.1039/d0ta01741h.

[74] T. Fujii, K. Toyoura, T. Uda, S. Kasamatsu, Theoretical study on proton diffusivity in Y-doped $BaZrO_3$ with realistic dopant configurations, Phys. Chem. Chem. Phys. 23 (2021) 5908, http://dx.doi.org/10.1039/D0CP06035F.

[75] P.G. Sundell, M.E. Bjorketun, G. Wahnstrom, Thermodynamics of doping and vacancy formation in $BaZrO_3$ perovskite oxide from density functional calculations, Phys. Rev. B 73 (2006) 104112, http://dx.doi.org/10.1103/PhysRevB.73.104112.

[76] M.P. Anderson, A.S. Nowick, Relaxation peaks produced by defect complexes in cerium dioxide doped with trivalent cations, J. Phys. Colloq. 42 (1981) C5–823, http://dx.doi.org/10.1051/jphyscol:19815128.

[77] M. Weller, A. Lakki, Defects in cubic zirconia studied by mechanical loss spectroscopy, Ber. Bunsenges. Phys. Chem. 101 (1997) 1297, http://dx.doi.org/10.1002/bbpc.199700042.

[78] A. Loken, T.S. Bjorheim, R. Haugsrud, The pivotal role of the dopant choice on the thermodynamics of hydration and associations in proton conducting $BaCe_{0.9}X_{0.1}O_{3-d}$ (X=Sc, Ga, Y, In, Gd and Er), J. Mater. Chem. A 3 (2015) 23289, http://dx.doi.org/10.1039/C5TA04932F.

[79] D.Y. Wang, A.S. Nowick, Dielectric relaxation in yttria-doped ceria solid solutions, J. Phys. Chem. Sol. 44 (1983) 639–646, http://dx.doi.org/10.1016/0022-3697(83)90110-5.

[80] R. Cantelli, F.M. Mazzolai, M. Nuovo, Internal friction due to long-range diffusion of hydrogen and deuterium in vanadium, J. Phys. Chem. Solids 31 (1970) 1811, http://dx.doi.org/10.1016/0022-3697(70)90172-1.

[81] M. Hein, A. Bals, A.F. Privalov, H. Wipf, Gorsky effect study of H and D diffusion in V and Ti at high H(D) concentrations, J. Alloys Compd. 356–357 (2003) 318, http://dx.doi.org/10.1016/S0925-8388(03)00111-7.

[82] H.R. Sinning, Mechanical damping by intercrystalline diffusion of hydrogen in metallic polycrystals, Phys. Rev. Lett. 85 (2000) 3201, http://dx.doi.org/10.1103/PhysRevLett.85.3201.

[83] L.P. Putilov, V.I. Tsidilkovski, Impact of bound ionic defects on the hydration of acceptor-doped proton-conducting perovskites check for updates, Phys. Chem. Chem. Phys. 21 (2019) 6391, http://dx.doi.org/10.1039/C8CP07745B.

[84] N.H. Chan, D.M. Smyth, Defect chemistry of donor-doped $BaTiO_3$, J. Am. Ceram. Soc. 67 (1984) 285, http://dx.doi.org/10.1111/j.1151-2916.1984.tb18849.x.

[85] A. Bonkowski, M.J. Wolf, J. Wu, S.C. Parker, A. Klein, R.A.D. Souza, A single model for the thermodynamics and kinetics of metal exsolution from perovskite oxides, J. Am. Chem. Soc. 146 (2024) 23012, http://dx.doi.org/10.1021/jacs.4c03412.

[86] Y. Wen, A. Rosnes, B. Jiang, O. Prytz, T. Norby, R. Haugsrud, J.M. Polfus, Nickel-induced lattice defects limit proton uptake in barium zirconate electrolytes, J. Am. Chem. Soc. 148 (2026) 379, http://dx.doi.org/10.1021/jacs.5c13935.

[87] G. Gregori, R. Merkle, J. Maier, Ion conduction and redistribution at grain boundaries in oxide systems, Prog. Mater. Sci. 89 (2017) 252, http://dx.doi.org/10.1016/j.pmatsci.2017.04.009.

[88] M. Kindelmann, I. Povstugar, S. Kuffer, D. Jennings, J.N. Ebert, M.L. Weber, M.P. Zahler, S. Escolastico, L. Almar, J.M. Serra, P. Kaghazchi, M. Bram, W. Rheinheimer, J. Mayer, O. Guillon, Controlling grain boundary segregation to tune the conductivity of ceramic proton conductors, Adv. Energy Mater. 15 (2025) 2404410, http://dx.doi.org/10.1002/aenm.202404410.

[89] R.A. McKnight, C.J. Howard, M.A. Carpenter, Elastic anomalies associated with transformation sequences in perovskites: I. Strontium zirconate, $SrZrO_3$, J. Phys. : Condens. Matter 21 (2009) 015901.

[90] L. Malavasi, C. Tealdi, C. Ritter, V. Pomjakushin, F. Gozzo, Y. Diaz-Fernandez, Combined neutron and synchrotron X-ray diffraction investigation of the $BaCe_{0.85-x}Zr_xY0.15O_{3-\delta}$ ($0.1 \leq \delta \leq 0.4$) proton conductors, Chem. Mater. 23 (2011) 1323.

[91] K. Nomura, H. Shimada, Y. Yamaguchi, W. Shin, Y. Okuyama, Y. Mizutani, Phase transitions and thermal expansions and chemical expansions and CO_2 resistances of $Ba(Ce_{0.8-x}Zr_xY_{0.1}Yb_{0.1})O_{3-d}$ (x= 0.1, 0.4) perovskite-type proton conductors, J. Electrochem. Soc. 169 (2022) 024516, http://dx.doi.org/10.1149/1945-7111/ac5480.

[92] F. Cordero, F. Trequattrini, F. Craciun, C. Galassi, Octahedral tilting, monoclinic phase and the phase diagram of PZT, J. Phys. : Condens. Matter 23 (2011) 415901, http://dx.doi.org/10.1088/0953-8984/23/41/415901.

[93] F. Cordero, F. Craciun, F. Trequattrini, C. Galassi, Effects of coupling between octahedral tilting and polar modes on the phase diagram of the ferroelectric perovskites $PbZr_{1-x}Ti_xO_3$ and $(Na_{1/2}Bi_{1/2})_{1-x}Ba_xTiO_3$, Phase Transit. 87 (2014) 255, http://dx.doi.org/10.1080/01411594.2013.796590.